

Emergent altermagnetism at surfaces of antiferromagnets: full symmetry classification and material identification

Colin Lange ,¹ Rodrigo Jaeschke-Ubiergo ,¹ Atasi Chakraborty ,¹ Xanthe H. Verbeek ,¹ Libor Šmejkal ,^{2,3} Jairo Sinova ,^{1,4} and Alexander Mook ,⁵

¹*Institute of Physics, Johannes Gutenberg University Mainz, 55099 Mainz, Germany*

²*Max Planck Institute for the Physics of Complex Systems, 01187 Dresden, Germany*

³*Max Planck Institute for Chemical Physics of Solids, 01187 Dresden, Germany*

⁴*Department of Physics, Texas A&M University, College Station, Texas 77843-4242, USA*

⁵*University of Münster, Institute of Solid State Theory, 48149 Münster, Germany*

We demonstrate the emergence of altermagnetism at the surfaces of antiferromagnets, vastly expanding the number of material candidates with altermagnetic characteristics and establishing a route to two-dimensional altermagnetism through surface-induced symmetry breaking. We do so by developing a *surface spin group* formalism that fully classifies all surface magnetic states and identifies altermagnetic surface spin groups that can arise at the surfaces of antiferromagnets. We use this formalism to identify over 140 antiferromagnetic entries from the MAGNDATA database with at least one altermagnetic surface, often times with multiple such surfaces in the same material. We illustrate this emergent phenomenon in a realistic Lieb lattice-based minimal model and present ab initio calculations on two representative material candidates, NaMnP and FeGe_2 , exhibiting d -wave and g -wave surface altermagnetism, respectively. Our theory naturally resolves the contradiction of recent experimental reports of d -wave ARPES measurements on metallic Lieb lattice compounds that have been shown to be antiferromagnetic in the bulk. Hence, we establish a new paradigm for generating two-dimensional altermagnetism by functionalizing the abundant material class of collinear antiferromagnets as viable platforms for controlled surface altermagnetism, creating natural materials for future hybrid device implementation.

I. Introduction

The recently discovered altermagnets (AMs) are magnetically compensated collinear ordered materials, with an unconventional time reversal symmetry (TRS) broken electronic band structure, characterized by an even-wave spin-splitting pattern with d -, g - or i -wave symmetry [1, 2]. This new unconventional magnetic phase completes the landscape of collinear magnets together with the well-known conventional ferromagnets (FMs) and antiferromagnets (AFMs) [1–4]. The full classification of bulk collinear magnets in these three types was achieved by considering their spin group symmetries, which allows for distinct symmetries acting on the spin texture and the lattice separately [5, 6]. The symmetry properties of altermagnets lead to several spintronics effects, such as anisotropic spin-polarized currents, anomalous Hall effect, and the novel spin-splitter effect [7]. While bulk altermagnetism has been experimentally verified in several materials, such as MnTe and CrSb [8–19], as well as in the metallic $\text{KV}_2\text{Se}_2\text{O}$ [20] and $\text{Rb}_{1-\delta}\text{V}_2\text{Te}_2\text{O}$ [21], there remains an interest in expanding the material class of experimentally readily available altermagnets. This is most relevant in the realm of 2D AMs, since most data technology applications are driven by interface effects. In addition, there is a growing number of interesting effects arising at altermagnetic interfaces, such as the interplay between altermagnetism and topological superconductivity [22, 23], edge- and cornertronics [24, 25], altermagnetic skyrmions [26, 27], as well as field switchable ferroelectric altermagnets [28–31] just to mention a few. Most existing strategies to generate 2D AMs focus on exfoliation from bulk AMs [32–35], bringing an extra step of complication because not all materials are easily exfoliable.

Given the motivation for 2D altermagnetism, we turn our attention to the largest class of magnetic materials, namely

collinear AFMs – with about 40% of materials in the MAGNDATA material database [36] belonging to this class [37]. A fundamental question is whether it is possible to functionalize AFMs in such a way that they generate altermagnetism. Here we demonstrate that this functionalization is possible through the symmetry breaking induced by the termination of particular AFMs in specific directions, i.e., emergent surface-induced altermagnetism in bulk AFMs. We do so by developing a spin group based theory of *surface spin groups* from which we create a systematic algorithm to fully classify all the surfaces of bulk AFMs and identify the ones having altermagnetic symmetries. This formalism is specific to a semi-infinite geometry with surface states, living in the 3D real-space and 2D momentum-space, which is different from the spin symmetries in the 3D [6] and strictly 2D monolayer systems [38, 39]. We apply this classification to the known collinear AFMs in the MAGNDATA database entries, identifying over 140 AFMs entries in this database with at least one spin-split altermagnetic surface. This new approach gives a general route to 2D AMs that vastly expands the pool of experimentally accessible AMs, eliminating the need for exfoliation, thereby avoiding the associated material and fabrication challenges.

These altermagnetic states at AFM surfaces can be directly probed by several surface sensitive experimental probes, such as spin-polarized scanning tunnel microscopy, angle resolved photoemission spectroscopy, and magneto-optical Kerr effect. Specifically, the recent reports of neutron scattering experiments on $\text{KV}_2\text{Se}_2\text{O}$ demonstrating a bulk antiferromagnetic order [40] and seemingly contradicting the surface-sensitive ARPES altermagnetic measurements [20], are naturally explained by our theory of surface altermagnetism. In addition, if these surface altermagnetic states are metallic, they can also exhibit transport properties specific to AMs (or FMs), such as the anomalous Hall effect [41, 42] and TMR [43, 44] or the

spin-splitter effect which is exclusive to AMs.

To visualize the intuition of surface-induced altermagnetism, in Sec. II, we first show this explicitly in a minimal tight-binding model of an AFM in a stacking geometry, taking inspiration from real materials in the Lieb lattice family. The calculated spin-resolved spectral density reveals directly the altermagnetic character of the surface states.

In Sec. III we present the symmetry-based algorithm identifying surface altermagnetism, where we develop the *surface spin groups* and, in particular, *surface spin Laue groups*, which enable the determination and classification of all magnetic surfaces in a given magnetic material. We isolate the surfaces that produce altermagnetic symmetries. Applying our methodology to the MAGNDATA database [36], we identify numerous AFMs as promising candidates that can exhibit surface altermagnetism (SAM). We also indicate AFMs with surfaces that have altermagnetic symmetries but where the surface plane coincides with one of the nodal planes of the altermagnetic order, making the surface electronic band structure spin degenerate. We term this scenario spin-degenerate surface altermagnetism (SD-SAM), reserving SAM for the spin-split surface altermagnetism explicitly. The full list of AFMs extracted from the MAGNDATA database that allow for SAM and SD-SAM is presented in the Appendix, identifying the specific AFMs and the different surfaces with their corresponding magnetic character. In Sec. IV, we present explicit ab initio calculation on two representative AFMs identified by our classification, NaMnP and FeGe₂, which exhibit *d*-wave and *g*-wave spin-split surface altermagnetism (SAM), respectively.

In Sec. V we discuss the implications of our general formalism to realize 2D altermagnetism through the controlled termination of bulk AFMs, specifically commenting on relevant current experimental debates on the above experiments on Lieb lattice materials, and possible pathways to new physics. In Sec. VI we present our conclusions and outlook on this new approach to engineer surface altermagnetism.

II. Minimal model for emergent surface altermagnetism

The inverse Lieb lattice [45–47] has attracted considerable attention as a minimal and conceptually clean platform to achieve two-dimensional *d*-wave altermagnetism. In the first report of two-dimensional altermagnetism, a single monolayer of FeSe [32], a parent compound of extensively studied FeSe-based superconductors, was shown to recover the same checkerboard order with altermagnetic symmetry, after breaking the inversion center that connects the opposite-spin Fe sites. In the same work, the magneto-optical Kerr effect was calculated as a probe of the time-reversal symmetry breaking at the surface of an FeSe slab system. Additionally, recent experimental reports on the metallic Lieb lattice compounds Rb_{1- δ} V₂Te₂O [21] and KV₂Se₂O [20] suggest altermagnetic order with *d*-wave symmetry at room temperature, but may in fact be explained by surface altermagnetism, as suggested by recent neutron scattering measurements indicating bulk antiferromagnetic order [40]. Both materials are of particular relevance to our discussion because the altermagnetic spin splitting was probed by spin- and angle-resolved photoemission spectroscopy, which directly accesses the states at the surface of the sample.

In the aforementioned family of materials, the bulk magnetic order depends on the stacking sequence of consecutive Lieb-lattice layers. When identical magnetic layers are stacked directly on top of each other, as was assumed in the reported experiments of KV₂Se₂O [20] and Rb_{1- δ} V₂Te₂O [21], the system is altermagnetic. By contrast, when the layers are stacked with alternating crystal environments, as in the representative structure shown in Fig. 1(a), the resulting system recovers the symmetries of an antiferromagnet.

We borrow intuition from this material class, and we write a minimal model that illustrates the symmetry-breaking mechanism behind the surface-induced altermagnetism. Later, in Sec. IV A, we will demonstrate the same effect in a closely related structure, in the antiferromagnetic NaMnP [48]. Our tight-binding model depicted in Fig. 1(a) consists of coupled layers, with each layer being a prototypical two-dimensional *d*-wave AM with checkerboard pattern. Red and blue spheres indicate the magnetic sites with opposite magnetic moment, characterized in the model by a Hund's coupling constant J . The altermagnetism in a single layer emerges from the presence of the nonmagnetic sites (denoted by a yellow sphere) which break the inversion center between opposite-spin sublattices within the same layer. Focusing on a given sublattice (red or blue), the intra-sublattice bonds along the [100] and [010] directions are inequivalent due to the presence of a nonmagnetic ligand along only one of these directions.

We integrate out the degrees of freedom associated with the yellow ligands, which in real materials can occupy a different Wyckoff position, and we introduce the resulting sublattice anisotropy through intra-sublattice hopping amplitudes $t_{2,a}$ and $t_{2,b}$, with $t_{2,a} \neq t_{2,b}$. These intra-sublattice hoppings alternate between adjacent layers, leading to a conventional antiferromagnetic order. Specifically, this alternation introduces the spin symmetry $[\mathcal{T}||\mathcal{PT}]$, which we abbreviate as \mathcal{PT} , with \mathcal{P} and \mathcal{T} denoting the real-space inversion, and the time-reversal symmetry, respectively. This \mathcal{PT} symmetry protects the spin degeneracy across the entire Brillouin zone. Here, the double bar $||$ separates the spin and real space operations. We also introduce a nearest neighbor inter-sublattice hopping amplitude t_1 , which is identical in every layer.

We wish to engineer surface states that preserve the altermagnetic properties of a single layer at the antiferromagnet's surface. To this end we introduce alternating vertical inter-layer couplings u and v , i.e., an SSH-type staggering of the hopping amplitudes [49]. The SSH inter-layer couplings $u \neq v$ break the center of inversion at the nonmagnetic ligand. Because of this, the real space inversion only connects opposite-spin sublattices [see Fig. 1(a)], and $[E||\mathcal{P}]$ is not a symmetry. However, the spin-only group of a collinear magnet, $\mathbf{r}_{\text{so}} = \text{SO}(2) \times \mathbb{Z}_2^{[C_{2\perp} \mathcal{T}||\mathcal{T}]}$, introduces an effective inversion in the electronic band structure [1]. Here, $C_{2\perp}$ is a two-fold spin rotation around an axis perpendicular to the collinear axis of the spins and E denotes the identity. The corresponding spin point group after introducing inversion is called the spin Laue group, and for this model reads

$$\mathbb{Z}_2^{[C_{2\perp}||E]} \times 1^4/1^m 1^m 1^m, \quad (1)$$

where $\mathbb{Z}_2^{[C_{2\perp}||E]} = \{[E||E], [C_{2\perp}||E]\}$. We adopt the notation

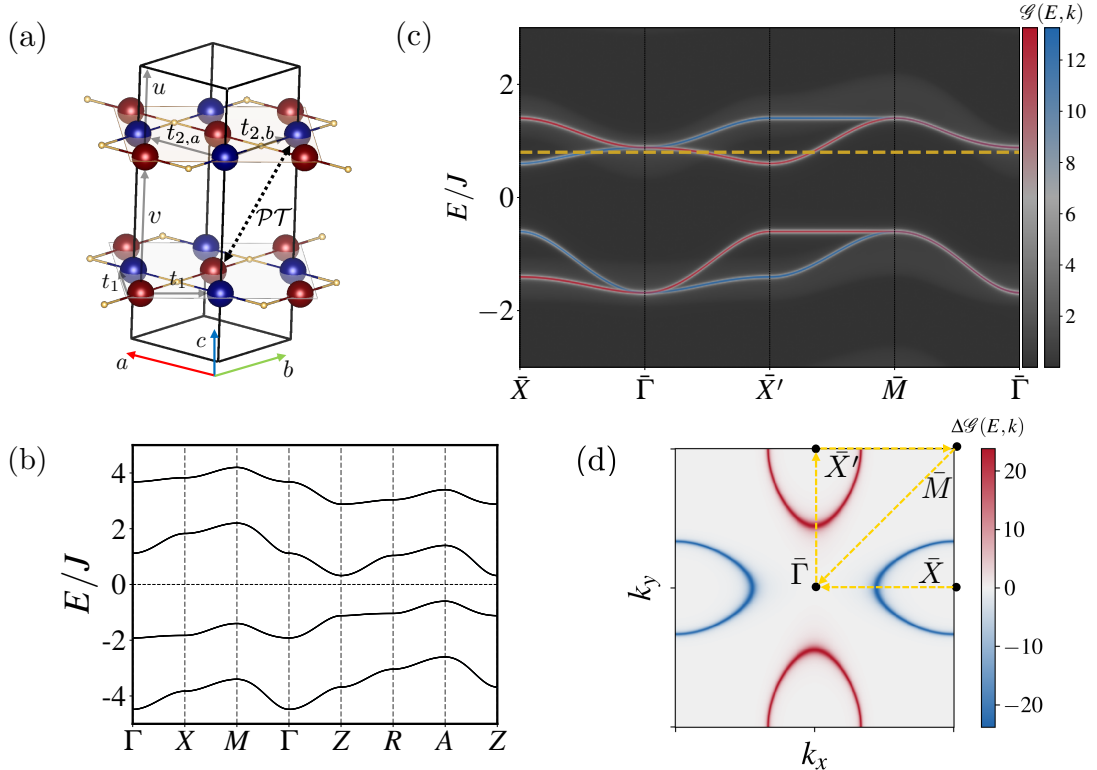


FIG. 1. Minimal model inspired by the layered Lieb lattice compounds. (a) Schematic of the crystal structure for a generic layered Lieb lattice system with the hoppings of the tight-binding model in Eq. (2) indicated. (b) Kramers' degenerate bulk bands of the minimal model with periodic boundary conditions in all three spatial directions. (c) Spin-resolved surface spectral density at the (001) surface showing altermagnetic splitting emerging from the surface-induced symmetry breaking. Red and blue colors depict spectral weight in the spin-up and down channels, respectively. The mixed color signifies the degeneracy of both channels in their spectral density. (d) Isoenergy cut of the difference between the spin-up and down channel of the surface spectral density in the two-dimensional surface Brillouin zone at $0.8/J$ [see dashed yellow line in (c)], exhibiting a d -wave pattern of the spin-splitting. Parameters in units of J read: $t_1 = 0.2$, $t_{2,a} = 0.4$, $t_{2,b} = 0$, $u = 1.2$, $J = 1$, $v = 0.4$.

introduced by Litvin [5, 6]. In this convention, the symbol $14/1m^1m^1m$ denotes the spin point group constructed from the crystallographic point group $4/mmm$ (Hermann–Mauguin notation) by associating a spin operation with each real-space symmetry generator. The superscript preceding each symbol specifies the corresponding spin operation. In particular, superscripts 1 and 2 denote the identity operation and a two-fold spin rotation about an axis perpendicular to the collinear spins, respectively.

The resulting Bloch Hamilton matrix is given by

$$\begin{aligned} \mathcal{H}_k = & [v - 2u \cos(k_z)] \sigma_x \otimes \tau_0 \otimes \nu_0 \\ & - 2u \sin(k_z) \sigma_y \otimes \tau_0 \otimes \nu_0 - t'(\mathbf{k}) \sigma_0 \otimes \tau_x \otimes \nu_0 \\ & - J \sigma_0 \otimes \tau_z \otimes \nu_z - (\mathcal{A}(\mathbf{k}) - \mathcal{B}(\mathbf{k})) \sigma_z \otimes \tau_z \otimes \nu_0 \\ & - (\mathcal{A}(\mathbf{k}) + \mathcal{B}(\mathbf{k})) \sigma_0 \otimes \tau_0 \otimes \nu_0, \end{aligned} \quad (2)$$

where σ_μ , τ_μ , and ν_μ with $\mu \in \{0, x, y, z\}$ are the Pauli matrices denoting the layer, the sublattice, and the spin degree of

freedom of the electrons, respectively. We have further defined

$$\begin{aligned} \mathcal{A}(\mathbf{k}) &= t_{2,b} \cos(k_x) + t_{2,a} \cos(k_y), \\ \mathcal{B}(\mathbf{k}) &= t_{2,a} \cos(k_x) + t_{2,b} \cos(k_y), \\ t'(\mathbf{k}) &= t_1 \cos\left(\frac{1}{2}(k_x + k_y)\right) + t_1 \cos\left(\frac{1}{2}(k_y - k_x)\right). \end{aligned} \quad (3)$$

The corresponding electronic band structure of this bulk AFM model is shown in Fig. 1(b). The presence of the \mathcal{PT} symmetry enforces the Kramers' degeneracy of the bands.

To resolve the states at the (001) *surface* of a semi-infinite version of this model, we use the established surface Green's function renormalization method [50–52]. It provides access to the spin-resolved spectral function $\mathcal{G}_\sigma(E, \mathbf{k}) = -\text{ImTr}G_\sigma(E, \mathbf{k})/\pi$ where $G_\sigma(E, \mathbf{k})$ is the surface Green's function with spin $\sigma = \uparrow, \downarrow$. In Fig. 1(c), we plot the overlaid $\mathcal{G}_\uparrow(E, \mathbf{k})$ and $\mathcal{G}_\downarrow(E, \mathbf{k})$ along a high-symmetry momentum path in the surface Brillouin zone. One can clearly see the high spectral weight of surface states with alternating spin polarization. The d -wave spin splitting in the surface spectrum becomes particularly clear for the isoenergy cut of $\Delta\mathcal{G}(E, \mathbf{k}) = \mathcal{G}(E, \mathbf{k}) - \mathcal{G}_\downarrow(E, \mathbf{k})$ shown in Fig. 1(d)

The spin point group of the bulk,

$$\mathbb{Z}_2^{[C_{2\perp}||E]} \times {}^14/{}^1m\, {}^1m\, {}^1m = [E||4/mmm] + [C_{2\perp}||4/mmm],$$

is broken down to

$${}^24/{}^1m\, {}^1m\, {}^2m = [E||mmm] + [C_{2\perp}||4/mmm - mmm]$$

by the termination of the (001) surface. Here, $4/mmm - mmm$ denotes the set difference between groups $4/mmm$ and mmm . Note that both groups are centrosymmetric (i.e., they are spin Laue groups), despite the fact that inversion symmetry is broken by the surface. This is because the collinearity of the spins induces an effective inversion in the electronic band structure, originating from the spin-only group [1].

The spin point group ${}^24/{}^1m\, {}^1m\, {}^2m$ corresponds to a d -wave altermagnet [1] (and reciprocal space group 6 from Ref. [39]). The symmetry $[C_{2\perp}||C_{4z}]$, with C_{4z} a four-fold rotational axis parallel to z that passes through the nonmagnetic ligand [yellow sphere in Fig. 1(a)], connects opposite-spin sublattices, and is reflected in the sign change of the spin-polarized surface spectral function under a 90° rotation [see path $\bar{X}\bar{\Gamma}\bar{X}'$ in Fig. 1(c)]. Additional sublattice transposing symmetries are the mirrors $[C_{2\perp}||m_{[110]}]$ and $[C_{2\perp}||m_{[1\bar{1}0]}]$. These transposing mirrors enforce two spin-degenerate nodal planes, which become nodal lines in the projected 2D surface Brillouin zone [see $\bar{\Gamma}\bar{M}$ path in Fig. 1(c,d)].

This minimal model, inspired by the broad family of materials with a layered structure of Lieb lattices, aims to illustrate a simple mechanism of how altermagnetism can emerge at the surface of an antiferromagnet: The symmetries enforcing spin degeneracy throughout the bulk Brillouin zone (here: \mathcal{PT} symmetry) are broken by the surface termination of the AFM, while some spin symmetries that protect the magnetic compensation are preserved.

III. Systematic search for surface altermagnetism

A natural next step is to develop a systematic strategy for identifying real materials that host surface altermagnetism. Establishing the appropriate mathematical framework, together with an algorithmic approach for its detection, serves two complementary purposes. First, it enables a complete classification of all symmetry scenarios in which surface altermagnetism can, in principle, arise. Second, it allows us to perform database searches of magnetic materials to identify concrete candidates and to compile statistics on the prevalence of bulk antiferromagnets exhibiting surface altermagnetism. We will proceed in three steps: (i) we define and discuss the mathematical objects of *surface* spin groups in Sec. III A. (ii) We classify surface spin groups describing altermagnetism in Sec. III B. (iii) We develop an algorithm to identify bulk AFM with surface altermagnetism in the MAGNDATA materials database in Sec. III C. Finally, (iv) we present its results to demonstrate the abundance of surface altermagnets in Sec. III D.

A. Definition of surface spin groups

We introduce the notion of a *surface* spin space group (sSSG), a notion that extends the spin-group framework [5, 6] to semi-infinite systems – similar to what the magnetic surface group

formalism in Ref. [53] provided for magnetic groups. We propose that the sSSG is the natural object for investigating exchange-dominated physics in experiments that resolve electronic states localized at the surface of the sample.

We define the nontrivial sSSG with respect to a nontrivial bulk SSG R^s and a surface normal \mathbf{n} as

$$R_{\mathbf{n}}^s = \{[g_s||g_r|\mathbf{t}] \in R^s : (g_r \cdot \mathbf{n} = \mathbf{n}) \wedge (\mathbf{t} \perp \mathbf{n})\}, \quad (4)$$

where g_s and g_r are point symmetries acting on spin and real space, respectively, and \mathbf{t} is a translation in direct space. Therefore, $[g_s||g_r|\mathbf{t}]$ is an element of the nontrivial bulk SSG R^s . For brevity, we will refer to $R_{\mathbf{n}}^s$ as the sSSG and drop the prefix “nontrivial”; this is justified by the fact that the spin-only group is always unaffected by the surface in real space. Note that $R_{\mathbf{n}}^s$ is a subgroup of R^s . Specifically, $R_{\mathbf{n}}^s$ comprises all elements of the bulk SSG that keep the normal \mathbf{n} of a given surface invariant and either (i) have no translational component at all, or (ii) involve translations purely within the surface plane (normal to \mathbf{n}).

In the remainder of this work, we restrict our analysis to spin *point* group elements within the surface spin point group (sSPG). To obtain those from the elements of the sSSG, we project out the translational part of each symmetry operation, identifying it with the corresponding point group transformation. We use the symbols \mathcal{R}^s and $\mathcal{R}_{\mathbf{n}}^s$ to denote the spin point group and sSPG associated with the bulk spin space group R^s and sSSG $R_{\mathbf{n}}^s$, respectively.

In order to appreciate in what way the sSPG differs from the more familiar SPG in 3D systems [6] and strict 2D monolayer systems [38, 39], we recapitulate how the latter two are constructed. There, one employs three- or two-dimensional representations in both real *and* reciprocal space. In contrast, since sSPG are meant to describe a semi-infinite system, the real space operations remain three-dimensional, but the Brillouin zone is projected onto only two dimensions, i.e., the surface Brillouin zone.

Next, we explain how this difference enters on a technical level. In 3D systems, the spin point group element $[C_{2\perp}||E]$ enforces spin degeneracy across the entire Brillouin zone [1]. Additionally, for collinear systems, the symmetry $[C_{2\perp}||\mathcal{P}]$ together with $[C_{2\perp}\mathcal{T}||\mathcal{T}] \in \mathbf{r}_{so}$ [5] implies the presence of $[\mathcal{T}||\mathcal{PT}]$ that enforces spin degeneracy even when SOC is included, because of Kramers’ theorem [1, 54, 55]. In the strict 2D limit, there are two additional elements, $[C_{2\perp}||m_n]$ and $[C_{2\perp}||C_n]$, which analogously enforce spin-degeneracy for collinear magnets [38, 39]. However, for semi-infinite systems with a surface, only $[C_{2\perp}||C_n]$ can be part of the nontrivial sSPG because $[C_{2\perp}||m_n]$ and $[C_{2\perp}||\mathcal{P}]$ by definition do not leave the normal of the respective surface invariant. This is the central distinguishing feature of the sSPG from both the well-established 3D SPG [1] and the 2D spin layer point groups [39]: Only the elements $[C_{2\perp}||E]$ and $[C_{2\perp}||C_n]$ give rise to spin-degenerate bands (the latter assuming collinear spins), placing sSPG in an intermediate regime between the fully three- and two-dimensional limits.

TABLE I. Classification of altermagnetic surface spin point groups. The first column specifies the partial-wave character associated with the surface spin group, that can be d -, g -, i -wave [1] or spin degenerate (SD-SAM). The second and third columns list the surface spin point group \mathcal{R}_n^s and the corresponding surface spin Laue group $\mathbb{Z}_2^{[E||\mathcal{P}]} \times \mathcal{R}_n^s$, respectively. These spin groups are given in Litvin notation [6]. The coordinate system is chosen such that z is parallel to the surface normal and x, y span the surface plane. The fourth column indicates whether the corresponding group generates spin splitting in the 2D surface Brillouin zone. A tick (\checkmark) indicates spin-split surface bands. These groups describe surface altermagnetism (SAM). In contrast, a cross (\times) denotes the absence of spin-splitting in the non-relativistic limit. These groups describe spin-degenerate surface altermagnetism (SD-SAM). The final column reports the number of surfaces of the respective symmetry group identified in our materials search of the MAGNCDATA database (see Tab. II). For consistency with the color-code used in Tab. II, those surface spin Laue groups in the third column that lead to spin-split surface states (SAM) are written in blue.

Surf. partial-wave character	Surf. spin point group	Surf. spin Laue group	Spin split surf. states?	No. of surfaces
d -wave	$^2m_x^2m_y^12_z$	$^2m_x^2m_y^1m_z$	\checkmark	131
	$^{24}2m^1m$	$^{24/1}m^2m^1m$	\checkmark	79
	24	$^{24/1}m$	\checkmark	1
	$^2m_{x/y}$	$^22_{x/y}^2m_{x/y}$	\checkmark	56
g -wave	$^{14}2m^2m$	$^{14/1}m^2m^2m$	\checkmark	2
i -wave	$^{16}2m^2m$	$^{16/1}m^2m^2m$	\checkmark	—
	$^{13}2m$	$^{1\bar{3}}2m$	\checkmark	1
SD-SAM	$^2m_{x/y}^1m_{y/x}2^2z$	$^2m_{x/y}^1m_{y/x}2m_z$	\times	284
	22_z	$^22_z^2m_z$	\times	59
	$^{26}2m^1m$	$^{26/2}m^2m^1m$	\times	—
	26	$^{26/2}m$	\times	1

B. Classification of altermagnetic surface spin groups

As in 3D and 2D spin groups, only specific surface spin groups support altermagnetism. These groups can be further classified according to the nodal structure they impose on the spin splitting of the altermagnetic surface, yielding d -, g -, and i -wave types characterized by two, four, and six nodal lines, respectively. In contrast to three-dimensional spin groups – but in close analogy with two-dimensional spin groups [56] – surface spin groups occur in two distinct variants, depending on whether the surface coincides with a nodal plane of the altermagnetic order. When the surface does not coincide with a nodal plane, the surface electronic spectrum is spin split, as expected for altermagnets; we refer to this case as surface altermagnetism (SAM). If, however, the surface lies within a nodal plane, the surface spin group still exhibits altermagnetic symmetries, yet the surface spectrum remains spin degenerate. We denote this latter scenario as spin-degenerate surface altermagnetism (SD-SAM). The full classification is presented in Tab. I. In the following, we will explain this table as we fill in the technical details.

Recall the definition of \mathcal{R}_n^s as the nontrivial sSPG associated with the nontrivial surface spin space group R_n^s in Eq. (4). Again, for brevity, we will drop the prefix “nontrivial” from here on when it is clear which group we mean. In order to identify altermagnetic sSPG, we first investigate the spatial parent point groups without spin information, i.e., the projection of the sSPG on the spatial part. In the following, when we say “groups”, we imply that we are talking about point groups.

Our strategy to end up with a full classification of all spin *Laue* groups starts by eliminating from the 32 crystallographic point groups all groups that are *not* viable surface point groups.

After that we analyze which spin Laue groups can be produced by the remaining spatial point groups. We do so by adding the effective inversion symmetry of the collinear spin-only group back to the nontrivial sSPG to generate the corresponding surface spin Laue group. As a final step, we discuss which of the surface spin Laue groups belong to the SAM class or to the SD-SAM class, based on their action on the electronic band structure.

We realize that all centrosymmetric groups and those generated by a roto-inversion (such as $\bar{4}$) cannot be a spatial parent of a sSPG because all inversions (and rotoinversions) do not leave any normal invariant. The second restriction is that there ought to be only one rotation axis present in the surface point group, because any two perpendicular rotation axes would not leave any normal invariant. For example, this restriction renders the point group 222 an impossible parent group for surface groups. Likewise, the identity trivially cannot support SAM or SD-SAM and is thus also not included. Taking these points into consideration, we are left with the following 9 candidates for spatial parent groups for the sSPG:

$$\{2, m, mm2, 4, 4mm, 3, 3m, 6, 6mm\}. \quad (5)$$

It is now necessary to add the spin information back because the directions of the symmetry axis associated with compensating symmetries are essential to distinguish between the SAM and SD-SAM classes. We note that in principle all groups in Eq. (5) can also support an *antiferromagnetic* surface if the symmetry $[C_{2\perp}||E]$ is present at the surface. As before, this arises from the projection of a spin translation element $[C_{2\perp}||E|\tau]$. At the level of the surface spin Laue group, this then produces the generic form $\mathbb{Z}_2^{[C_{2\perp}||E]} \times \mathcal{G}$, where \mathcal{G} is one of

the point groups mentioned above. Because in this manuscript we focus on altermagnetic surfaces, we will not discuss this situation further.

Without loss of generality, and for notational simplicity, we assume throughout this discussion that the surface normal is along the z direction, with the x and y directions lying in the surface plane. Following the convention in Ref. [1], we choose $\{E, C_{2\perp}\}$ as the spin parent group for the construction of the collinear spin groups. Because this spin parent group has two elements, every subgroup of the full product group between the spin and the spatial parent group can be built from halving subgroups of the spatial parent. This is the particular case of Litvin's theorem for binary spin parent groups [5, 6].

We now move to different combinations of the aforementioned spin parent group with the 9 spatial parent point groups in Eq. (5) and go through the list one-by-one:

(1) We start with the group 2_z . (We indicate the z in the subscript because we have chosen the z axis as the surface normal.) This group only has the trivial subgroup that generates the nontrivial sSPG 22_z .

(2) The same argument applies to the group m where now the normal has to be inside the mirror plane, generating $^2m_{x/y}$. The parent point group m_z , however, is *not* eligible because it does not leave the normal in z invariant. From here on, we will *not* mention orientations of symmetry elements that are forbidden due to the restriction of the sSPG and instead only discuss cases that actually work.

(3) The group $mm2$ has three viable halving subgroups, namely, m_x , m_y , and 2_z . So, we can have two distinct nontrivial sSPG from this; they are $^2m_{x/y}^2m_{y/x}^12_z$ and $^2m_{x/y}^1m_{y/x}^22_z$, where we have again used the fact that the rotation axis must be parallel to the normal.

(4) The group 4 has only one halving subgroup, 2 , so we get only one nontrivial sSPG: 24_z .

(5) The group $4mmm$ has 4 and $mm2$ as halving subgroups, generating the two nontrivial spin point groups $^24^1m^2m$ (\cong $^24^2m^1m$) and $^14^2m^2m$, where again, only one rotation axis is allowed, which must be parallel to the normal of the surface.

(6) The group 3 is a special case because it does not have a halving subgroup. Thus it cannot support AM or SD-SAM and is thus ruled out.

(7) In contrast, $3m$ has only one halving subgroup, which is 3 and generates the nontrivial sSPG $^13^2m$.

(8) The group 6 only has 3 as a halving subgroup, generating the nontrivial sSPG 26 .

(9) Finally, the group $6mm$, similar to $4mm$, has one halving subgroup generated by the rotations and two isomorphic ones generated by the mirror. Thus, we get the nontrivial sSPG $^26^2m^1m$ and $^16^2m^2m$.

We conclude that there are in total the following 11 different nontrivial sSPG:

$$\left\{ \begin{array}{l} ^22_z, ^2m_{x/y}, ^2m_{x/y}^2m_{y/x}^12_z, ^2m_{x/y}^1m_{y/x}^22_z, ^24_z, \\ ^24^1m^2m, ^14^2m^2m, ^13^2m, ^26, ^26^2m^1m, ^16^2m^2m \end{array} \right\},$$

which are listed in the second column of Tab. I.

We now add the effective inversion symmetry of the spin-only group to build surface spin Laue groups from this. This

step produces the following list:

$$\left\{ \begin{array}{l} ^22_z/2m, ^22/2^2m_{x/y}, ^2m_{x/y}^2m_{y/x}^1m_z, \\ ^2m_{x/y}^1m_{y/x}^2m_z, ^24_z/1m, ^24_z/1m^1m^2m, \\ ^14_z/1m^2m^2m, ^1\bar{3}^2m, ^26/2m, ^26/2m^2m^1m, ^16/1m^2m^2m \end{array} \right\}.$$

These 11 surface spin Laue groups of the form $\mathbb{Z}^{[E||\mathcal{P}]} \times \mathcal{R}_n^s$ correspond to the 11 groups listed in the third column of Tab. I.

In the first column of Tab. I, we list the partial-wave character, constrained by the surface spin Laue group. We order the possible groups as d -, g -, and i -wave [1]. When analyzing the spin-splitting symmetry that each of these groups imposes, one should note that, due to the 2D nature of the projected Brillouin zone (surface Brillouin zone), in the spin split cases (see 4th column in Tab. I), there will be spin-degenerate nodal *lines* instead of nodal planes. All of them are forced to be straight lines, with the only exception of the spin Laue group $^24/1m$, in which the symmetry $[C_{2\perp}||C_{4z}]$ enforces two spin unpolarized curves ("nodal curves") that cross the Γ point, but do not have to be straight. The surface partial-wave character of almost all surface spin Laue groups, is directly inherited from the 3D spin point groups [1], with two exceptions: (i) the SD-SAM cases, discussed in the next paragraph; and (ii) the group $^1\bar{3}^2m$, which in three dimensions exhibits g -wave symmetry, characterized by three spin degenerate nodal planes and one generally curved nodal surface. Upon projection to two dimensions, this partial-wave structure yields an i -wave spin-splitting pattern with six nodal lines: three originating from the nodal planes and three arising from the intersection of the curved nodal surface with the $k_z = 0$ plane [32].

Regarding the question of the groups describing SAM or SD-SAM, we focus on the compensating two-fold rotation axis $[C_{2\perp}||C_{2n}]$ because it generates a compensating *mirror* in the plane of the surface when considering the associated Laue group. Since the Brillouin zone gets projected onto two dimensions (i.e., onto the surface Brillouin zone spanned in the xy -plane) we get under the action of the spin Laue group element

$$[C_{2\perp}||m_z]\epsilon(s, k_x, k_y) = \epsilon(-s, k_x, k_y) \stackrel{!}{=} \epsilon(s, k_x, k_y),$$

which implies spin degeneracy of the bands $\epsilon(s, k_x, k_y)$, where ϵ denotes energy and s spin. The groups that have (that do *not* have) this spin-group element are labeled with "X" ("✓") in the fourth column of Tab. I. The checkmark and the cross therefore, indicate if the electronic surface spectrum is spin split (✓) or not (X).

Note that although SD-SAM surfaces do not display the characteristic alternating spin splitting in momentum space in the non-relativistic limit, they *do not* have time reversal as a point symmetry (as opposed to *antiferromagnetic* surfaces). Despite the 2D nature of the surface Brillouin zone, in real space, the spin density is still a three-dimensional object, which implies that there is a ferroic order of the partial-wave components of the atomic spin density, with characteristic d - or g -wave symmetry [57–59]. SD-SAM cannot have i -wave symmetry.

C. Search algorithm for surface altermagnets

With all altermagnetic surface groups classified (see Sec. III B and Tab. I), we now turn to the question of how to identify the surface spin Laue group of a specific surface of a specific material. To develop such an algorithm, first, note that choosing a generic crystal direction as a normal \mathbf{n} of the surface will only generate the trivial sSSG, which is not altermagnetic, because it lacks any compensating symmetry; instead, it should be considered a ferromagnetic, uncompensated surface. We therefore have to apply filters as to what normals are sensible candidates.

We restrict ourselves to surfaces whose normals are symmetry axes of the bulk SSG, that is, normals that are left invariant by certain operations of the bulk SSG. For example, consider again the minimal model in Sec. II and investigate it from the perspective of the sSSG. As stated in Sec. II, the symmetry group of the bulk system is given by $\mathbb{Z}_2^{[C_{2\perp}||E]} \times 14/1m^1m^1m$. Consider terminating the bulk of the minimal model in the $\mathbf{n} \parallel [001]$ direction. Clearly, the sublattice-transposing four-fold rotation and the orthogonal mirrors (which come both as sublattice-transposing and nontransposing) leave \mathbf{n} invariant. Thus, the corresponding nontrivial sSPG of the bulk system terminated in the [001] direction is 24^1m^2m . If we then go to the surface spin Laue group, by adding the effective inversion of the spin-only group, we arrive at $24^1m^1m^2m$. According to the third row in Tab. I, we conclude that the [001] surface of the minimal model is a d -wave SAM surface. The expected d -wave spin splitting is evident from the explicit calculations carried out in Sec. II (recall Fig. 1). Other surface normals of the minimal model that are left invariant under some bulk SSG operations are [100] and [010]. Their sSPG is $1m^2m^22_n$. This group, and thus the corresponding surface spin Laue group $1m^2m^2m$, has the element $[C_{2\perp}||C_{2n}]$. Therefore, these are SD-SAM surfaces (see second row in Tab. I).

We now take this intuition from the minimal model and turn to the systematic analysis of *all* conventional collinear 3D antiferromagnets in the MAGNDATA database. Our algorithm works as follows:

When looping over all entries in the MAGNDATA database, we first check if they are collinear and then determine their *bulk* spin Laue group. If it is antiferromagnetic [1], then this material is a candidate for our surface analysis. (Note that this step excludes, in particular, bulk altermagnets.) If a material has passed the previous test, we find a finite set \mathcal{N} of candidate surface normals \mathbf{n} that are left invariant under a subset of symmetries of the material's space group.

For each surface normal $\mathbf{n} \in \mathcal{N}$, we calculate the nontrivial sSSG R_n^s and identify the corresponding nontrivial sSPG \mathcal{R}_n^s . Next, we calculate the surface spin Laue group $\mathbb{Z}^{[E||\mathcal{P}]} \times \mathcal{R}_n^s$, which takes into account the effective inversion symmetry of the spin-only group for collinear magnets. At this point, we are able to identify from the surface spin Laue group if the surface is ferromagnetic (magnetically uncompensated), antiferromagnetic, or altermagnetic – if the latter, we use Tab. I to determine the symmetry type of altermagnetism. As a last step, we check for the element $[C_{2\perp}||C_{2n}]$ in the surface spin Laue group to decide whether the group describes SAM or

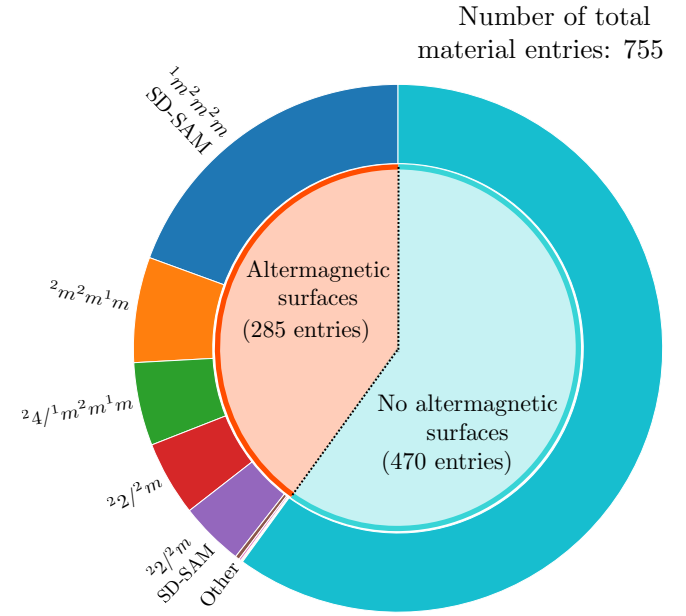


FIG. 2. Pie chart summarizing the results of the surface altermagnetism screening of the MAGNDATA database, consisting of 755 total entries that are 3D AFMs. The inner pie chart shows the share of materials that have altermagnetic surfaces, i.e., SAM or SD-SAM surfaces. The outer pie chart shows the shares of the respective surface spin Laue groups. Notice that it is common among the materials with altermagnetic surfaces to have multiple different surfaces with SAM/SD-SAM surface spin Laue groups. The “Other” category encompasses the surface spin Laue groups $1\bar{3}2m$, $2\bar{6}2m$, $14/1m^2m^2m$, and $24/1m$. The total number of surfaces for the respective surface spin Laue group is given in Tab. I.

SD-SAM.

D. List of surface altermagnet candidates in MAGNDATA database

The results of the screening of the MAGNDATA database [36] are summarized in Fig. 2. We identified 755 materials entries in the MAGNDATA database as collinear 3D AFMs. This step was done by direct determination of the spin space groups [60] of the magnetic structures reported by neutron scattering experiments. While all materials trivially have some uncompensated, i.e., ferromagnetic, surfaces, we do not discuss these here, since our interest lies in compensated magnetic surfaces. Of those with compensated surfaces, we find 141 materials entries that exhibit at least one SAM surface and 186 materials entries that exhibit at least one SD-SAM surface. There are many materials that have multiple compensated surfaces and show different sSSG that are SAM, SD-SAM, or antiferromagnetic in the same material. For each of the 11 surface spin Laue groups, we indicate in the last column of Tab. I how many surfaces of this type in the MAGNDATA materials entries we have found, with d -wave SAM and SD-SAM being the dominating type of surface altermagnetism. The detailed list of MAGNDATA materials entries with altermagnetic surfaces is shown in Appendix B in Tab. II, including NaMnP and FeGe₂, the two compounds we address by first-principles

calculations below in Sec. IV.

Given the extent of the materials list provided in Tab. II in Appendix B, it is worthwhile to comment on certain characteristic materials. Interestingly, the collinear tetragonal phase of Mn_3Pt [61] – a well known non-collinear AFM at lower temperatures – supports *d*-wave character SAM on its [001] surfaces. Within the screened database, only SrRu_2O_6 [62] supports *i*-wave SAM at its [001] surface, and only the [001] surface of $\text{KTb}_3\text{F}_{12}$ [63] has the surface spin Laue group $^{24/1}m$ with generally curved nodal paths. Other materials of note are, for example, the magnetoelectric Cr_2O_3 [64], and the prototypical materials from antiferromagnetic spintronics, Mn_2Au [65] and CuMnAs [66], where Mn_2Au is a prominent example of the SD-SAM case with four surfaces of this type.

There are multiple superconducting parent compounds with altermagnetic surfaces, such as the (010) surface of PrFeAsO [67], which exhibits *d*-wave SAM. Also, La_2CuO_4 [68] in its AFM phase exhibits SD-SAM in its (010) surface – note that for La_2CuO_4 an AM phase has also been reported [69]. These compounds are particularly interesting from the perspective of interface and proximity effects, some of which have been studied in the context of the interplay between superconductivity and altermagnetism for generating spin-triplet Cooper pairs [70].

IV. Characteristic material candidates

From the materials listed in Table II, we focus on two representative examples to demonstrate how surface altermagnetism is borne out in first-principles calculations. Specifically, we consider the \mathcal{PT} -symmetric antiferromagnets NaMnP [48] (MAGNDATA entries No. 0.626–0.628, Table II entries 191–193) and FeGe_2 [71] (MAGNDATA entry No. 1.557, Table II entry 122). NaMnP exhibits a *d*-wave surface spin polarization, whereas FeGe_2 presents an example of *g*-wave texture in the surface spin splitting. The Néel temperatures of the antiferromagnetic NaMnP and FeGe_2 are reported to be >293 K [48] and ~ 315 K [71] respectively. Below, we discuss the bulk and surface characteristics for these two individual materials candidates from an *ab initio* perspective. The specific computational details of the first principles calculations can be found in Appendix A.

A. *D*-wave surface altermagnetism in NaMnP

NaMnP is a bulk antiferromagnetic semiconductor with collinear compensated magnetic moments on the Mn atoms [48, 72], see Fig. 3(a). This ordering has a magnetic point group $4'/m'm'm$. NaMnP crystallizes with space group $P4/nmm$, where the Mn atoms sit on Wyckoff position 2a (0, 0, 0), and the Na and P on position 2c ($\frac{1}{2}, 0, z$). The crystal structure is closely related to the previously discussed Lieb lattice. However, in this case, the nonmagnetic ligands *do not* break the center of inversion that connects the two oppositely spin-polarized Mn sublattices, as illustrated by the inset in Fig. 3(b). As a result, the crystal structure more closely resembles the symmetry of FeSe [32]. The orientation of the ligand pyramids in NaMnP breaks $\mathcal{T}t$ symmetry, making NaMnP a bulk \mathcal{PT} antiferromagnet. As a consequence, Kramers' spin degeneracy is preserved for the bulk bands ev-

erywhere in momentum space, as can be seen in the spin-polarized band structure we computed in the non-relativistic limit in Fig. 3(b). Our *ab initio* calculations yield a magnetic moment of $3.51 \mu_B$ per Mn site, in good agreement with the experimentally reported moment of magnitude $3.64 \mu_B$ [71].

Clearly, the symmetry that preserves the effective TRS is broken when terminating the material in the [001] or in the [1 $\bar{1}0$] (and [110]) directions. However, the effect of the surface termination on the other symmetries differs between the two surfaces. The surface with normal $\hat{n} \parallel [001]$, preserves some of the rotational symmetries of the bulk, including the $[C_{2\perp}||C_{4z}]$ symmetry, resulting in the surface spin Laue group $^{24/1}m^1m^2m$. We demonstrate the distinct nature of the surface by studying the spectral function $\mathcal{G}_\sigma(E, \mathbf{k})$ of the spin-up ($\sigma = \uparrow$) and spin-down ($\sigma = \downarrow$) polarized bands at the surface. It is given by $\mathcal{G}_\sigma(E, \mathbf{k}) = -\text{ImTr}G_\sigma(E, \mathbf{k})/\pi$, where $G_\sigma(E, \mathbf{k})$ is the surface Green's function of the respective spin channel σ . For the surface with normal $\hat{n} \parallel [001]$, we choose the Mn atom termination and show $\mathcal{G}_\sigma(E, \mathbf{k})$ in Fig. 3(c,d), for the spin-up and spin-down channels, respectively. Here, the white shaded region predominantly captures the bulk contribution to the spectral functions, which is equal in both channels, while the red and blue regions indicate the surface states, which are distinct. Furthermore, in Fig. 3(e), we show the difference in the spectral function between the two polarizations, i.e., $\Delta\mathcal{G}(E, \mathbf{k}) = \mathcal{G}_\uparrow(E, \mathbf{k}) - \mathcal{G}_\downarrow(E, \mathbf{k})$, for the (001) surface, again with the surface termination of Mn atoms. This difference spectral function shows the strong polarization with the expected *d*-wave nature, with two nodal lines, which are protected by the spin symmetries $[C_{2\perp}||m_{[110]}]$ and $[C_{2\perp}||m_{[1\bar{1}0]}]$. The difference spectral function changes sign under a four-fold rotation, as expected from the symmetry $[C_{2\perp}||C_{4z}]$ of the 2D surface. We note that for a surface with the same normal, but termination with the nonmagnetic P and Na atoms, we find a similar effect with identical symmetry. The surface with normal $\hat{n} \parallel [1\bar{1}0]$ only preserves two mirrors, and breaks the four-fold rotational symmetry, resulting in the surface spin Laue group $^{2m^2m^1m}$ and a different *d*-wave character than the (001) termination. We show the difference spectral function for this surface termination in Fig. 3(f), with the axes rotated such that z' indicates the surface normal (and $k_{x'}$ and $k_{y'}$ span the surface). Again, we see the clear *d*-wave nature, with two nodal planes which are protected by the spin symmetries $[C_{2\perp}||m_{x'}]$ and $[C_{2\perp}||m_{y'}]$, but here without the four-fold rotational symmetry.

B. *G*-wave surface altermagnetism in FeGe_2

The second candidate material FeGe_2 [see Fig. 4 (a)] provides a representative example for the realization of *g*-wave surface altermagnetism. It crystallizes in the tetragonal $I4/mcm$ space group [71], with Fe and Ge atoms occupying the Wyckoff positions 4a (0, 0, $\frac{1}{2}$) and 8h ($x, x + \frac{1}{2}, \frac{1}{4}$), respectively. The bulk magnetic ground state is a collinear antiferromagnetic configuration belonging to the magnetic point group $mmm1'$, which preserves \mathcal{PT} symmetry. We have computed the spin-polarized band structure in the non-relativistic limit in Fig. 4(b). Our *ab initio* GGA calculations yield a magnetic moment of $1.53 \mu_B$ per Fe site, in good agreement with the

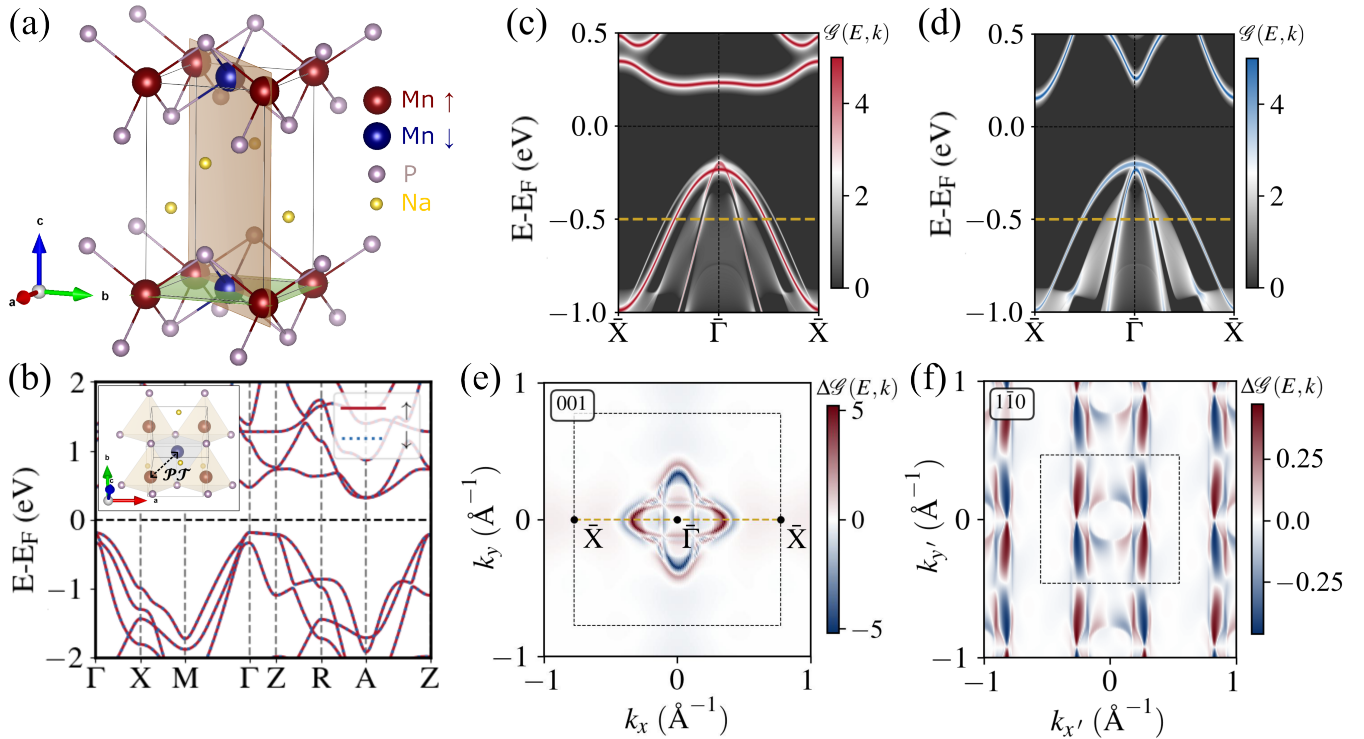


FIG. 3. Candidate material NaMnP for a \mathcal{PT} AFM that exhibits d -wave altermagnetic surface states. (a) Crystal unit cell showing compensated collinear magnetic ordering of Mn moments. Two different termination planes (001) and (110) are indicated in green and brown. Surface spin group analysis predicts d -wave altermagnetic surface states for (001) and (110), respectively, but with different surface spin Laue groups. (b) Spin-polarized bulk electronic bands calculated without spin-orbit coupling (SOC), showing Kramers' spin degeneracy. Inset highlights how the \mathcal{PT} symmetry connects the two sublattices in the bulk. (c) Spin-up and (d) spin-down channel spectral function ($\mathcal{G}(E, \mathbf{k})$) without SOC of the (001) Mn-terminated surface, indicated with the green plane in (a), showing both bulk and surface states along the path $\bar{\Gamma}$ (0,0,0)– \bar{X} (0.5,0,0), indicated by a yellow line in panel (e) in the the surface Brillouin zone. (e) The spin-polarized spectral function difference ($\Delta\mathcal{G}(E, \mathbf{k}) = \mathcal{G}_\uparrow(E, \mathbf{k}) - \mathcal{G}_\downarrow(E, \mathbf{k})$) at $E_F - 0.5$ eV for (001) termination exhibiting d -wave nature with two nodal planes, and rotational symmetry. Surface Brillouin zone indicated with a black dashed square. (f) The spectral function difference for the two spin channels calculated for (110) termination at $E_F - 0.5$ eV, with the axes system rotated such that $k_{z'}$ parallel to the surface normal, exhibiting d -wave nature with two nodal surfaces without rotational symmetry, and with surface Brillouin zone indicated with black dashed rectangle.

experimentally reported effective moment of $1.21 \mu_B$ [71]. Consistent with bulk \mathcal{PT} symmetry, Kramers' degeneracy is preserved across the entire Brillouin zone, as evident from the bulk band structure shown in Fig. 4(b). The \mathcal{PT} partners of magnetic Fe sublattices are shown in the inset of Fig. 4(b).

Applying symmetry arguments analogous to those previously discussed for the d -wave surface altermagnet NaMnP, we predict that FeGe₂ supports a g -wave altermagnetic surface state for a (001) surface termination. The bulk magnetic structure has the spin symmetry $[C_{2\perp}||m_x|t_b]$, with $t_b = [0, \frac{1}{2}, 0]$, which connects opposite-spin Fe sublattices, as shown in Fig. 4(a). This glide mirror, together with three additional glide mirrors normal to [110], [110] and [010], is preserved under the (001) surface termination, and lead to the surface spin Laue group $^{14}/1m^2m^2m$. The material-specific schematic of the semi-infinite geometry is depicted in the right panel of Fig. 4(a). We again have calculated the spectral functions $\mathcal{G}(E, \mathbf{k})$ at the $\hat{\mathbf{n}} \parallel [001]$ Fe terminated surface in Fig. 4(c,d) for spin-up and spin-down channels, respectively, in the non-relativistic limit. While the bulk

spectral function (white shaded region) remains identical for both spin channels, the surface states (red and blue) exhibit spin-dependent momentum dispersion. As with NaMnP, to characterize the symmetry of the surface spin-polarization, we show the difference of the spin-resolved spectral functions, $\Delta\mathcal{G}(E, \mathbf{k}) = \mathcal{G}_\uparrow(E, \mathbf{k}) - \mathcal{G}_\downarrow(E, \mathbf{k})$, in Fig. 4(e) for the (001) termination. The resulting pattern reveals a clear g -wave texture in the 2D surface Brillouin zone with nodal lines coinciding with mirrors m_x , m_y , m_{110} , and $m_{1\bar{1}0}$ contained within the surface spin Laue group $^{14}/1m^2m^2m$. For another choice of consecutive Fe termination, the g -wave texture remains the same but reverses its sign. This sign reversal of the texture can be understood from the fact that the local environments of two successive Fe layers with opposite spins are related by a $[C_{2\perp}||C_{2y}|t_b]$ symmetry (two-fold rotation in spin-space, combined with a two-fold screw axis in real space). Notably, the altermagnetic g -wave texture of $\Delta\mathcal{G}(E, \mathbf{k})$ is robust against different surface terminations, whether by magnetic Fe layer or nonmagnetic Ge layer.

To further validate our symmetry-based analysis in a realistic

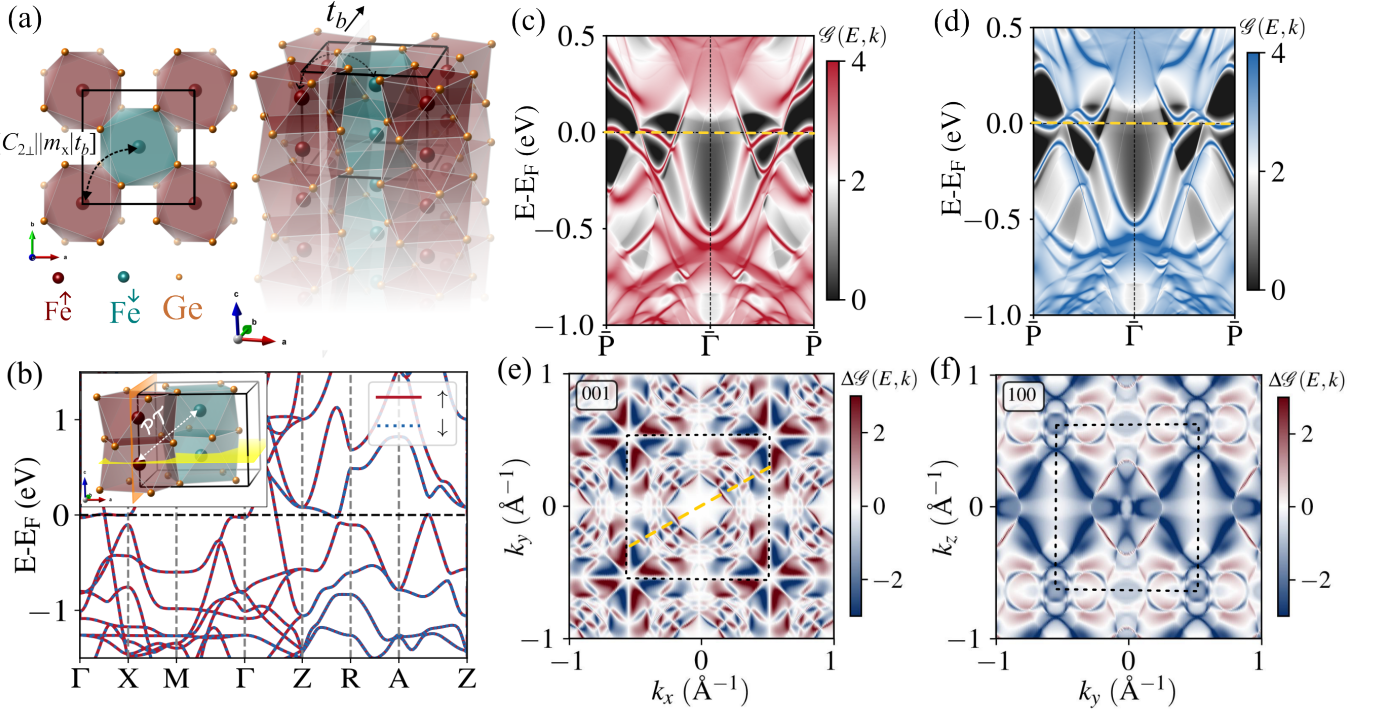


FIG. 4. Candidate material FeGe_2 for a \mathcal{PT} AFM that exhibits g -wave altermagnetic surface states. (a) Left panel: Top view of the crystal unit cell showing antiparallel magnetic ordering of Fe moments, indicating the $[C_{2\perp}||m_x|t_b]$ spin transposing symmetry, where $t_b = (0, \frac{1}{2}, 0)$. Right panel: Terminated bulk structure, showing the glide m_x plane. (b) Spin-polarized Kramers' degenerate bulk dispersion calculated without spin-orbit coupling (SOC). The \mathcal{PT} symmetric magnetic sublattices are shown in the inset. Spectral function ($\mathcal{G}(E, \mathbf{k})$) of the (001) Fe-terminated surface [shown with yellow plane in the inset of (b)] without SOC, showing both bulk and surface states for spin-up (c) and spin-down (d) channels, respectively. The spin splitting near the Fermi energy is ~ 0.08 eV along the path $\bar{\Gamma}$ (0,0,0)- \bar{P} (0.5,0.25), indicated by a dashed yellow line in panel (e) in the surface Brillouin zone (dashed black square). (e) The spin-polarized spectral function difference ($\Delta\mathcal{G}(E, \mathbf{k}) = \mathcal{G}_{\uparrow}(E, \mathbf{k}) - \mathcal{G}_{\downarrow}(E, \mathbf{k})$) at the Fermi energy for (001) termination exhibits g -wave nature with four nodal planes. (f) The spectral function difference for two spin channels calculated for (100) termination [shown with orange plane in the inset of (b)], indicating an uncompensated ferromagnetic nature in agreement with symmetry prediction.

setting, we have calculated $\Delta\mathcal{G}(E, \mathbf{k})$ for $\hat{n} \parallel [100]$ which does *not* support surface altermagnetism. The corresponding surface is shown in the inset of Fig. 4(b) by the orange plane. In this case, $\Delta\mathcal{G}(E, \mathbf{k})$ exhibits uncompensated or ferromagnetic character [see Fig. 4(f)] with one spin channel dominating the spectral weight for an Fe terminated $\hat{n} \parallel [100]$ surface, which is also in agreement with our symmetry based analysis.

V. Discussion

The emergent altermagnetism at the surfaces of antiferromagnets discussed above provides a natural route to reconciling the apparently conflicting reports on $\text{KV}_2\text{Se}_2\text{O}$. The angle-resolved photoemission spectroscopy (ARPES) data of Ref. [20] were interpreted in terms of *bulk* d -wave altermagnetism. However, this interpretation appears to be at odds with the neutron diffraction results of Ref. [40], which instead indicate a G -type antiferromagnetic order in the bulk, characterized by a $(0, 0, \frac{1}{2})$ propagation vector. Our results resolve this apparent discrepancy: ARPES is inherently surface sensitive, and the (001) surface of the proposed AFM order in $\text{KV}_2\text{Se}_2\text{O}$ would reduce the symmetry, allowing SAM characterized by the d -wave surface spin Laue group $^{24/1}m^1m^2m$

(which is the same as $^{24/1}m^2m^1m$ reported in Tab. I but with a rotated d -wave pattern). Hence, within our theory, the observation of d -wave altermagnetism by the surface-sensitive ARPES reported in Ref. [20] is perfectly compatible with the bulk antiferromagnetic order reported in Ref. [40]. In addition, since the ARPES observations on $\text{Rb}_{1-\delta}\text{V}_2\text{Te}_2\text{O}$ [21] have the same structure, if $\text{Rb}_{1-\delta}\text{V}_2\text{Te}_2\text{O}$ turns out to be an antiferromagnet in the bulk, our theory would also predict SAM of d -character in the experimental orientation.

Surface altermagnetism naturally opens up perspectives for interface and device physics. In particular, one may envision insulating three-dimensional antiferromagnets whose altermagnetic surface or interface states are metallic, forming a two-dimensional electron gas that is localized near the boundary. Since bulk charge transport is suppressed in such systems, the altermagnetic properties of the surface or interface would be directly accessible in transport measurements. For instance, a two-dimensional electron gas with d -wave altermagnetic symmetry is expected to exhibit the spin-splitter effect. More generally, the theoretical framework of surface spin groups introduced here can be directly extended to *interface spin groups*, allowing one to systematically describe the

combined spin symmetries of the interfaced materials together with the symmetry reduction intrinsic to the interface.

While SAM surfaces exhibit the characteristic beyond *s*-wave even-parity spin splittings of *d*-, *g*-, or *i*-wave symmetry, SD-SAM surfaces do not. In the nonrelativistic limit, their electronic bands remain spin-degenerate. The key distinction from antiferromagnetic surfaces is that SD-SAM surfaces lack time-reversal symmetry in their surface point group. We therefore argue that SD-SAM surfaces become particularly relevant once relativistic effects are taken into account: spin degeneracy is lifted throughout the surface Brillouin zone, except at specific high-symmetry points determined by the orientation of the Néel vector, thereby rendering time-reversal symmetry breaking explicitly observable. Two-dimensional material systems with this symmetry have recently been shown to exhibit an anomalous Hall effect [56]. SD-SAM surfaces – which may host sizable Rashba spin–orbit coupling due to structural inversion symmetry breaking at the surface – can thus be expected to display pronounced magneto-optical responses. In particular, the magneto-optical Kerr effect in reflection geometry is inherently surface sensitive and a natural probe of such states. In addition, in embedded interfaces with topological insulating materials, many effects would be greatly enhanced, and possible quantum anomalous Hall effect scenarios could be envisioned.

The interplay between altermagnetism and spin-orbit coupling is expected to be equally important for SAM surfaces. A prominent illustration of how these effects can conspire to yield unexpected spin symmetry properties is provided by the bulk altermagnet MnTe. In the nonrelativistic limit, MnTe realizes a *g*-wave altermagnetic phase dictated by its spin symmetries [1]. Upon inclusion of spin-orbit coupling, the broken time-reversal symmetry by the altermagnetic order produces a relativistic spin polarization orthogonal to the Néel order, on one of the nodal planes of the non-relativistic *g*-wave order, that has even parity (*d*-wave) and is time-reversal odd [8, 9]. By analogy, SAM surfaces of suitable materials may undergo a similar spin-orbit-coupling-induced transmutation of their effective altermagnetic symmetry. A systematic exploration of the interplay between SAM and relativistic effects is left for future work.

We reiterate that our analysis of emergent surface altermagnetism relies exclusively on the spin symmetry of the bulk parent magnetic phase. Of course, surfaces, depending on whether interfaced with vacuum or embedded in a heterostructure, can change their symmetry through structural relaxation (preserving the bulk unit cell at the surface) or reconstruction (changing the bulk unit cell at the surface), or through magnetic relaxation and reconstruction (e.g., due to surface-perturbed exchange mean fields or magnetic surface anisotropy). However, many surfaces in fact show only a few percent of relaxation in normal direction with negligible effect on the symmetry of the surface. Modern interface engineering techniques further enable precise control over surface termination and strain, allowing experimentalists to preserve bulk-derived symmetries in many systems. Although reconstructions – such as unit-cell doubling that could convert an antiferromagnetic surface into an altermagnetic one – are con-

ceivable, they are neither universal nor predictable from bulk symmetry alone; they depend sensitively on chemical bonding, termination, and preparation. In contrast, our framework identifies surface altermagnetism as a direct symmetry-based consequence of the bulk magnetic order that is independent of surface-specific chemistry or reconstruction. This makes our complete classification not only predictive but also foundational for the systematic functionalization of AFM in spintronic applications.

VI. Conclusion and Outlook

We have established a general and symmetry-driven pathway to realize two-dimensional altermagnetism through the controlled termination of bulk collinear antiferromagnets. By introducing the concept of surface spin groups and, in particular, surface spin Laue groups, we developed a systematic classification algorithm that identifies surfaces of antiferromagnets capable of hosting altermagnetic symmetries – either spin-split (SAM) or spin-degenerate (SD-SAM) – without requiring exfoliation or external field engineering. Applied to the MAGNDATA database [36], this approach reveals over 140 materials entries with at least one altermagnetic surface with spin splitting, vastly expanding the pool of experimentally accessible 2D altermagnet candidates.

Our minimal tight-binding model, inspired by layered Lieb-lattice systems, provides an intuitive proof of concept: surface termination in an otherwise conventional AFM can induce an even-wave spin-splitting pattern characteristic of altermagnetism. This is confirmed by *ab initio* calculations on two representative materials – NaMnP (*d*-wave SAM) and FeGe₂ (*g*-wave SAM) – which exhibit clear spin-resolved surface band structures with the predicted altermagnetic nodal topology.

This paradigm shift – from searching for bulk AMs or engineering 2D AMs via exfoliation or adsorption – to generating 2D AMs via surface termination of abundant AFMs, opens a scalable route toward experimental realization. Crucially, these surface states are directly accessible to surface-sensitive probes such as spin-polarized STM, ARPES, and magneto-optical Kerr effect, enabling unambiguous experimental verification.

We have also argued that the ARPES [20] and neutron scattering [40] measurements on KV₂Se₂O already contain signatures consistent with surface-induced altermagnetism in a bulk AFM. This raises a cautionary note: phenomena previously ascribed to intrinsic bulk altermagnetic order could instead originate from the surface.

In summary, emergent surface-induced altermagnetism provides not only a theoretical framework but also a practical materials design strategy to bridge the gap between the abundance of AFMs and the scarcity of experimentally viable 2D AMs. This approach promises to accelerate the discovery and deployment of altermagnetic materials in next-generation spintronic, quantum, and topological technologies.

Acknowledgments

This work was funded by the German Research Foundation (DFG) through TRR 173-268565370 (Projects No. A03 and B13), TRR 288-422213477 (Projects No. A09 and B05), and Project No. 504261060 (Emmy Noether Programme). We acknowledge support by the Dynamics and Topology Cen-

ter (TopDyn) funded by the State of Rhineland-Palatinate. LS acknowledges funding from the ERC Starting Grant No. 101165122. We also acknowledge the high-performance computational facility of the supercomputer “Mogon” at Johannes Gutenberg-Universität Mainz, Germany.

[1] L. Šmejkal, J. Sinova, and T. Jungwirth, *Physical Review X* **12**, 031042 (2022).

[2] L. Šmejkal, J. Sinova, and T. Jungwirth, *Physical Review X* **12**, 040501 (2022).

[3] T. Jungwirth, R. M. Fernandes, E. Fradkin, A. H. MacDonald, J. Sinova, and L. Šmejkal, *Newton* **1**, 100162 (2025).

[4] T. Jungwirth, J. Sinova, R. M. Fernandes, Q. Liu, H. Watanabe, S. Murakami, S. Nakatsuji, and L. Šmejkal, *Nature* **649**, 837 (2026).

[5] D. B. Litvin and W. Opechowski, *Physica* **76**, 538 (1974).

[6] D. B. Litvin, *Acta Crystallographica Section A* **33**, 279 (1977).

[7] T. Jungwirth, J. Sinova, P. Wadley, D. Kriegner, H. Reichlова, F. Krizek, H. Ohno, and L. Šmejkal, *Arxiv Preprint* (2025).

[8] J. Krempaský, L. Šmejkal, S. W. D’Souza, M. Hajlaoui, G. Springholz, K. Uhlířová, F. Alarab, P. C. Constantinou, V. Strocov, D. Usanov, W. R. Pudelko, R. González-Hernández, A. B. Hellenes, Z. Jansa, H. Reichlова, Z. Šobáň, R. D. G. Betancourt, P. Wadley, J. Sinova, D. Kriegner, J. Minár, J. H. Dil, and T. Jungwirth, *Nature* **626**, 517 (2024).

[9] S. S. Lee, S. S. Lee, S. Jung, J. Jung, D. Kim, Y. Lee, B. Seok, J. Kim, B. G. Park, L. Šmejkal, C.-J. Kang, and C. Kim, *Physical Review Letters* **132**, 036702 (2024).

[10] T. Osumi, S. Souma, T. Aoyama, K. Yamauchi, A. Honma, K. Nakayama, T. Takahashi, K. Ohgushi, and T. Sato, *Physical Review B* **109**, 115102 (2024).

[11] M. Hajlaoui, S. W. D’Souza, L. Šmejkal, D. Kriegner, G. Krizman, T. Zakušlo, N. Olszowska, O. Caha, J. Michalička, J. Sánchez-Barriga, A. Marmodoro, K. Výborný, A. Ernst, M. Cinchetti, J. Minár, T. Jungwirth, and G. Springholz, *Advanced Materials* **36**, 2314076 (2024).

[12] M. Chilcote, A. R. Mazza, Q. Lu, I. Gray, Q. Tian, Q. Deng, D. Moseley, A. Chen, J. Lapano, J. S. Gardner, G. Eres, T. Z. Ward, E. Feng, H. Cao, V. Lauter, M. A. McGuire, R. Hermann, D. Parker, M. Han, A. Kayani, G. Rimal, L. Wu, T. R. Charlton, R. G. Moore, and M. Brahlek, *Advanced Functional Materials* **34**, 2405829 (2024).

[13] O. J. Amin, A. D. Din, E. Golias, Y. Niu, A. Zakharov, S. C. Fromage, C. J. B. Fields, S. L. Heywood, R. B. Cousins, F. Maccherozzi, J. Krempaský, J. H. Dil, D. Kriegner, B. Kiraly, R. P. Campion, A. W. Rushforth, K. W. Edmonds, S. S. Dhesi, L. Šmejkal, T. Jungwirth, and P. Wadley, *Nature* **636**, 348 (2024).

[14] S. Reimers, L. Odenbreit, L. Šmejkal, V. N. Strocov, P. Constantinou, A. B. Hellenes, R. J. Ubiergo, W. H. Campos, V. K. Bharadwaj, A. Chakraborty, T. Denneulin, W. Shi, R. E. Dunin-Borkowski, S. Das, M. Kláui, J. Sinova, and M. Jourdan, *Nature Communications* **15**, 2116 (2024).

[15] G. Yang, Z. Li, S. Yang, J. Li, H. Zheng, W. Zhu, Z. Pan, Y. Xu, S. Cao, W. Zhao, A. Jana, J. Zhang, M. Ye, Y. Song, L.-H. Hu, L. Yang, J. Fujii, I. Vobornik, M. Shi, H. Yuan, Y. Zhang, Y. Xu, and Y. Liu, *Nature Communications* **16**, 1442 (2025).

[16] J. Ding, Z. Jiang, X. Chen, Z. Tao, Z. Liu, T. Li, J. Liu, J. Sun, J. Cheng, J. Liu, Y. Yang, R. Zhang, L. Deng, W. Jing, Y. Huang, Y. Shi, M. Ye, S. Qiao, Y. Wang, Y. Guo, D. Feng, and D. Shen, *Physical Review Letters* **133**, 206401 (2024).

[17] M. Zeng, M. Zhu, Y.-P. Zhu, X. Liu, X.-M. Ma, Y.-J. Hao, P. Liu, G. Qu, Y. Yang, Z. Jiang, K. Yamagami, M. Arita, X. Zhang, T.-H. Shao, Y. Dai, K. Shimada, Z. Liu, M. Ye, Y. Huang, Q. Liu, and C. Liu, *Advanced Science* **11**, 2406529 (2024).

[18] C. Li, M. Hu, Z. Li, Y. Wang, W. Chen, B. Thiagarajan, M. Leandersson, C. Polley, T. Kim, H. Liu, C. Fulga, M. G. Vergniory, O. Janson, O. Tjernberg, and J. van den Brink, *Arxiv Preprint* [10.48550/arXiv.2405.14777](https://arxiv.org/abs/2405.14777) (2024).

[19] Z. Liu, M. Ozeki, S. Asai, S. Itoh, and T. Masuda, *Physical Review Letters* **133**, 156702 (2024).

[20] B. Jiang, M. Hu, J. Bai, Z. Song, C. Mu, G. Qu, W. Li, W. Zhu, H. Pi, Z. Wei, Y.-J. Sun, Y. Huang, X. Zheng, Y. Peng, L. He, S. Li, J. Luo, Z. Li, G. Chen, H. Li, H. Weng, and T. Qian, *Nature Physics* **21**, 754 (2025).

[21] F. Zhang, X. Cheng, Z. Yin, C. Liu, L. Deng, Y. Qiao, Z. Shi, S. Zhang, J. Lin, Z. Liu, M. Ye, Y. Huang, X. Meng, C. Zhang, T. Okuda, K. Shimada, S. Cui, Y. Zhao, G.-H. Cao, S. Qiao, J. Liu, and C. Chen, *Nature Physics* **21**, 760 (2025).

[22] I. I. Mazin, *AAPPS Bulletin* **35**, 18 (2025).

[23] P. Chatterjee and V. Jurčić, *Arxiv Preprint* (2025).

[24] G. Yang, R. Chen, C. Liu, J. Li, Z. Pan, L. Deng, N. Zheng, Y. Tang, H. Zheng, W. Zhu, Y. Xu, X. Ma, X. Wang, S. Cui, Z. Sun, Z. Liu, M. Ye, C. Cao, M. Shi, L. Hu, Q. Liu, S. Qiao, G. Cao, Y. Song, and Y. Liu, *Arxiv Preprint* (2025).

[25] R. M. Sattigeri, X. Gong, A. Fakhredine, C. Autieri, and G. Cuono, *Arxiv Preprint* (2025).

[26] Z. Jin, Z. Zeng, Y. Cao, and P. Yan, *Physical Review Letters* **133**, 196701 (2024).

[27] K. Dou, Z. He, W. Du, Y. Dai, B. Huang, and Y. Ma, *Arxiv Preprint* (2025).

[28] L. Šmejkal, *Arxiv Preprint* (2024).

[29] M. Gu, Y. Liu, H. Zhu, K. Yananose, X. Chen, Y. Hu, A. Stroppa, and Q. Liu, *Physical Review Letters* **134**, 106802 (2025).

[30] D. Wang, H. Wang, L. Liu, J. Zhang, and H. Zhang, *Nano Letters* **498** (2024).

[31] H. Zhu, J. Li, X. Chen, Y. Yu, and Q. Liu, *Nature Communications* **16**, 4882 (2025).

[32] I. Mazin, R. González-Hernández, and L. Šmejkal, *Arxiv Preprint*, 1 (2023).

[33] N. Jana, A. Chakraborty, A. Mukherjee, and A. Agarwal, *Phys. Rev. B*, 075127 (2025).

[34] S.-D. Guo, *Arxiv Preprint* (2025).

[35] D. Liu, S. Zeng, J.-H. Liao, and Y.-J. Zhao, *Arxiv Preprint*.

[36] S. V. Gallego, J. M. Perez-Mato, L. Elcoro, E. S. Tasci, R. M. Hanson, K. Momma, M. I. Aroyo, and G. Madariaga, *J. Appl. Cryst.* **49**, 1750 (2016).

[37] X. Chen, J. Ren, Y. Zhu, Y. Yu, A. Zhang, P. Liu, J. Li, Y. Liu, C. Li, and Q. Liu, *Physical Review X* **14**, 031038 (2024).

[38] M. Tian, C. Cui, Z. Zhang, J. Duan, W. Feng, and R.-W. Zhang, *Arxiv Preprint* (2025).

[39] S. Zeng and Y. J. Zhao, *Physical Review B* **110**, 054406 (2024).

[40] Y. Sun, Y. Huang, J. Cheng, S. Zhang, Z. Li, H. Luo, X. Ma, W. Yang, J. Yang, D. Chen, K. Sun, M. Gutmann, S. C. Capelli, F. Shen, J. Hao, L. He, G. Chen, and S. Li, *Physical Review B* **112**, 184416 (2025).

[41] L. Šmejkal, A. H. MacDonald, J. Sinova, S. Nakatsuji, and T. Jungwirth, *Nature Reviews Materials* **7**, 482 (2022).

[42] Z. Feng, X. Zhou, L. Šmejkal, L. Wu, Z. Zhu, H. Guo, R. González-Hernández, X. Wang, H. Yan, P. Qin, X. Zhang, H. Wu, H. Chen, Z. Meng, L. Liu, Z. Xia, J. Sinova, T. Jungwirth, and Z. Liu, *Nature Electronics* **5**, 735 (2022).

[43] L. Šmejkal, A. B. Hellenes, R. González-Hernández, J. Sinova, and T. Jungwirth, *Physical Review X* **12**, 011028 (2022).

[44] S. Noh, G.-H. Kim, J. Lee, H. Jung, U. Seo, G. So, J. Lee, S. Lee, M. Park, S. Yang, Y. S. Oh, H. Jin, C. Sohn, and J.-W. Yoo, *Physical Review Letters* **134**, 246703 (2025).

[45] N. Kaushal and M. Franz, Arxiv Preprint [10.48550/arXiv.2412.16421](https://arxiv.org/abs/2412.16421) (2024).

[46] M. Dürrnagel, H. Hohmann, A. Maity, J. Seufert, M. Klett, L. Klebl, and R. Thomale, Arxiv Preprint (2024).

[47] P.-H. Chang, I. I. Mazin, and K. D. Belashchenko, Arxiv Preprint [1](https://arxiv.org/abs/2401.00001) (2025).

[48] W. Bronger, P. Müller, R. Höppner, and H. Schuster, *Zeitschrift für anorganische und allgemeine Chemie* **539**, 175 (1986).

[49] J. R. S. and A. J. Heeger W. P. Su, *Phys. Rev. Lett* **42**, 1698 (1979).

[50] M. P. L. Sancho, J. M. L. Sancho, and J. Rubio, *Journal of Physics F: Metal Physics* **14**, 1205 (1984).

[51] M. P. L. Sancho, J. M. L. Sancho, and J. Rubio, *Journal of Physics F: Metal Physics* **15**, 851 (1985).

[52] J. Henk and W. Schattke, *Computer Physics Communications* **77**, 69 (1993).

[53] S. F. Weber, A. Urru, S. Bhowal, C. Ederer, and N. A. Spaldin, *Physical Review X* **14**, 021033 (2024).

[54] H. A. Kramers, *Proc. Amsterdam Acad.* **33** (1930).

[55] E. Wigner, *Nachrichten von der Gesellschaft der Wissenschaften zu Göttingen, Mathematisch-Physikalische Klasse* **1932**, 546 (1932).

[56] L. Bai, R.-W. Zhang, W. Feng, and Y. Yao, Arxiv Preprint (2025).

[57] R. M. Fernandes, V. S. de Carvalho, T. Birol, and R. G. Pereira, *Physical Review B* **109**, 024404 (2024).

[58] P. A. McClarty and J. G. Rau, *Physical Review Letters* **132**, 176702 (2023).

[59] R. Jaeschke-Ubiergo, V.-K. Bharadwaj, W. Campos, R. Zarzuela, N. Biniskos, R. M. Fernandes, T. Jungwirth, J. Sinova, and L. Šmejkal, Arxiv Preprint (2025).

[60] K. Shinohara, A. Togo, H. Watanabe, T. Nomoto, I. Tanaka, and R. Arita, *Acta Crystallographica Section A Foundations and Advances* **80**, 94 (2024).

[61] E. Krén, G. Kádár, L. Pál, J. Sólyom, and P. Szabó, *Physics Letters* **20**, 331 (1966).

[62] W. Tian, C. Svoboda, M. Ochi, M. Matsuda, H. B. Cao, J.-G. Cheng, B. C. Sales, D. G. Mandrus, R. Arita, N. Trivedi, and J.-Q. Yan, *Physical Review B* **92**, 100404 (2015).

[63] M. Guillot, M. El-Ghazzi, D. Avignant, G. Andre, F. Bouree, and A. Cousson, *Journal of Applied Physics* **91**, 8519 (2002).

[64] M. Fiebig, D. Fröhlich, and H. J. Thiele, *Physical Review B* **54**, R12681 (1996).

[65] V. M. Barthem, C. V. Colin, H. Mayaffre, M. H. Julien, and D. Givord, *Nature Communications* **4**, 2892 (2013).

[66] M. H. Karigerasi, K. Kang, J. Huang, V. K. Peterson, K. C. Rule, A. J. Studer, A. Schleife, P. Y. Huang, and D. P. Shoemaker, *Physical Review Materials* **6**, 1 (2022).

[67] S. A. J. Kimber, D. N. Argyriou, F. Yokaichiya, K. Habicht, S. Gerischer, T. Hansen, T. Chatterji, R. Klingeler, C. Hess, G. Behr, A. Kondrat, and B. Büchner, *Physical Review B* **78**, 140503 (2008).

[68] M. Reehuis, C. Ulrich, K. Prokeš, A. Gozar, G. Blumberg, S. Komiya, Y. Ando, P. Pattison, and B. Keimer, *Physical Review B* **73**, 144513 (2006).

[69] C. Lane, J. W. Furness, I. G. Buda, Y. Zhang, R. S. Markiewicz, B. Barbiellini, J. Sun, and A. Bansil, *Physical Review B* **98**, 125140 (2018).

[70] D. Chakraborty and A. M. Black-Schaffer, Arxiv Preprint (2024).

[71] N. S. S. Murthy, R. J. Begum, C. S. Somanathan, and M. R. L. N. Murthy, *Solid State Communications* **3**, 113 (1965).

[72] Y. Chen, J. Ji, L. Hong, X. Wan, and H. Xiang, *Physical Review Letters* **135**, 146703 (2025).

[73] J. P. Perdew, K. Burke, and M. Ernzerhof, *Physical Review Letters* **77**, 3865 (1996).

[74] P. E. Blöchl, *Physical Review B* **50**, 17953 (1994).

[75] G. Kresse and D. Joubert, *Physical Review B* **59**, 1758 (1999).

[76] G. Kresse and J. Furthmüller, *Computational Materials Science* **6**, 15 (1996).

[77] N. Marzari and D. Vanderbilt, *Physical Review B* **56**, 12847 (1997), kES.

[78] A. A. Mostofi, J. R. Yates, G. Pizzi, Y. S. Lee, I. Souza, D. Vanderbilt, and N. Marzari, *Computer Physics Communications* **185**, 2309 (2014).

[79] Q. S. Wu, S. N. Zhang, H.-F. F. Song, M. Troyer, and A. A. Soluyanov, *Computer Physics Communications* **224**, 405 (2017).

[80] Magndata: A collection of magnetic structures with portable cif-type files.

A. Computational Details

We performed *ab initio* calculations using density functional theory (DFT) within the plane-wave basis. We used the Perdew-Burke-Ernzerhof (PBE) implementation of the generalized gradient approximation (GGA) for the exchange correlation functional [73], together with the projector augmented-wave potentials [74, 75] as implemented in the Vienna *ab initio* simulation package (VASP) [75, 76]. All calculations were performed without Coulomb correlation and without spin-orbit coupling. In our DFT calculations we chose kinetic energy cutoffs for the plane-wave basis of 800 eV for NaMnP and 550 eV for FeGe₂, respectively. Γ -centered k -point meshes of 12×12×7 (NaMnP) and 8×8×10 (FeGe₂) k -point meshes were used to perform the momentum space calculations for the Brillouin zone integration of the bulk systems. To calculate the surface spectral functions, we constructed the Wannier functions using the VASP2WANNIER90 [77] and WANNIER90 codes [78]. The low-energy tight-binding Hamiltonian was defined in an effective Wannier basis including only Na-s, Mn-d, and P-p for NaMnP, and Fe-d and Ge-p for FeGe₂, with all remaining degrees of freedom down-folded. Using the obtained tight-binding model, we calculate the surface spectral function for different terminations using the iterative Green's function method, as implemented in the WannierTools package [79].

B. List of surface altermagnet candidates in the MAGNDATA materials database

TABLE II: Results of the MAGNDATA [36, 80] database screening for three-dimensional AFM with altermagnetic surfaces. Material entries with only AFM or uncompensated surfaces are not included. All uncompensated surfaces for the listed material entries are omitted. The first column entitled “No.” enumerates the entries. The second column called “Material entry” provides the chemical formula of the compounds. The third column “Index” gives the MAGNDATA entry index. The forth column called “Normals” shows the normal vectors describing all compensated surfaces in the material. These normals are written in the coordinates spanned by the lattice vectors, with the crystal-setting convention used in MAGNDATA [36, 80]. The fifth column “Surface spin Laue group” denotes the surface spin Laue group for SAM and SD-SAM surfaces and the crystallographic surface Laue group for AFM surfaces. The surface spin Laue groups are given in Litvin’s notation [6]. SAM surface groups are colored blue, SD-SAM are colored black and AFM surface groups are colored lightgrey. For the surface spin Laue groups corresponding to AFMs (gray font), we list here a crystallographic point group \mathbf{G} , in such a way that the spin Laue group is given by $\mathbb{Z}_2^{[C_{2\perp}||E]} \times \mathbf{G} = [E||\mathbf{G}] + [C_{2\perp}||\mathbf{G}]$. The final column entitled “Surface character” gives the partial-wave character for SAMs, and reads AFM or SD-SAM in the other cases.

No.	Material entry	Index	Normals	Surf. spin Laue group	Surface character
1	AgNiO ₂	1.50	[001] [010]	$\bar{1}$ $^22_z/2m_z$	AFM SD-SAM
2	AgRuO ₃	0.733	[110] [100] [010]	$^22_z/2m_z$ $^22_z/2m_z$ $^22_z/2m_z$	SD-SAM SD-SAM SD-SAM
3	BaCoF ₄	1.439	[100] [001] [010]	$2/m$ $^2\bar{2}/^2m$ $\bar{1}$	AFM <i>d</i> -wave AFM
4	Ba ₃ CoRu ₂ O ₉	0.750	[001] [010] [100]	$2/m$ $^2m^1m^2m$ $^2m^2m^1m$	AFM SD-SAM <i>d</i> -wave
5	Ba ₃ CoRu ₂ O ₉	0.749	[001] [100] [010]	$2/m$ $^2m^2m^1m$ $^2m^1m^2m$	AFM <i>d</i> -wave SD-SAM
6	BaCoSO	1.594	[001] [100] [010]	$2/m$ $^2m^1m^2m$ $2/m$	AFM SD-SAM AFM
7	BaCoSO	1.593	[001] [100] [010]	$2/m$ $^2m^1m^2m$ $2/m$	AFM SD-SAM AFM
8	BaCo ₂ V ₂ O ₈	1.30	[001] [100] [010]	$^2m^1m^2m$ $^2m^1m^2m$ $^2m^1m^2m$	SD-SAM SD-SAM SD-SAM
9	BaCr ₂ As ₂	0.365	[001] [100] [110] [010] [110]	$^24/1m^1m^2m$ $^2m^1m^2m$ $^2m^2m^1m$ $^2m^1m^2m$ $^2m^2m^1m$	<i>d</i> -wave SD-SAM <i>d</i> -wave SD-SAM <i>d</i> -wave
10	BaCrFeAs ₂	0.366	[001] [100] [110] [010] [110]	$^24/1m^1m^2m$ $^2m^1m^2m$ $^2m^2m^1m$ $^2m^1m^2m$ $^2m^2m^1m$	<i>d</i> -wave SD-SAM <i>d</i> -wave SD-SAM <i>d</i> -wave

No.	Material entry	Index	Normals	Surface spin	Laue group	Surface character
11	BaFe ₂ O ₄	1.754	[001]	$2/m$	AFM	
			[010]	$2\bar{2}/2m$	<i>d</i> -wave	
			[100]	$2\bar{2}/2m$	<i>d</i> -wave	
12	Ba ₂ FeSi ₂ O ₇	1.641	[001]	$2m^2m^1m$	<i>d</i> -wave	
			[010]	$\bar{1}$	AFM	
			[110]	$2/m$	AFM	
			[100]	$\bar{1}$	AFM	
			[110]	$2/m$	AFM	
13	BaMn ₂ As ₂	0.18	[001]	$24/1m^1m^2m$	<i>d</i> -wave	
			[100]	$2m^1m^2m$	SD-SAM	
			[110]	$2m^2m^1m$	<i>d</i> -wave	
			[010]	$2m^1m^2m$	SD-SAM	
			[110]	$2m^2m^1m$	<i>d</i> -wave	
14	BaMn ₂ Bi ₂	0.89	[001]	$24/1m^1m^2m$	<i>d</i> -wave	
			[100]	$2m^1m^2m$	SD-SAM	
			[110]	$2m^2m^1m$	<i>d</i> -wave	
			[010]	$2m^1m^2m$	SD-SAM	
			[110]	$2m^2m^1m$	<i>d</i> -wave	
15	BaMn ₂ Ge ₂	0.606	[001]	$24/1m^1m^2m$	<i>d</i> -wave	
			[100]	$2m^1m^2m$	SD-SAM	
			[110]	$2m^2m^1m$	<i>d</i> -wave	
			[010]	$2m^1m^2m$	SD-SAM	
			[110]	$2m^2m^1m$	<i>d</i> -wave	
16	BaMn ₂ Ge ₂	0.605	[001]	$24/1m^1m^2m$	<i>d</i> -wave	
			[100]	$2m^1m^2m$	SD-SAM	
			[110]	$2m^2m^1m$	<i>d</i> -wave	
			[010]	$2m^1m^2m$	SD-SAM	
			[110]	$2m^2m^1m$	<i>d</i> -wave	
17	BaMn ₂ P ₂	0.464	[001]	$24/1m^1m^2m$	<i>d</i> -wave	
			[100]	$2m^1m^2m$	SD-SAM	
			[110]	$2m^2m^1m$	<i>d</i> -wave	
			[010]	$2m^1m^2m$	SD-SAM	
			[110]	$2m^2m^1m$	<i>d</i> -wave	
18	BaMnSb ₂	0.611	[001]	$24/1m^1m^2m$	<i>d</i> -wave	
			[100]	$2m^1m^2m$	SD-SAM	
			[110]	$2m^2m^1m$	<i>d</i> -wave	
			[010]	$2m^1m^2m$	SD-SAM	
			[110]	$2m^2m^1m$	<i>d</i> -wave	
19	BaMn ₂ Sb ₂	0.470	[001]	$24/1m^1m^2m$	<i>d</i> -wave	
			[100]	$2m^1m^2m$	SD-SAM	
			[110]	$2m^2m^1m$	<i>d</i> -wave	
			[010]	$2m^1m^2m$	SD-SAM	
			[110]	$2m^2m^1m$	<i>d</i> -wave	
20	Ba ₂ Mn ₃ Sb ₂ O ₂	0.471	[001]	$24/1m^1m^2m$	<i>d</i> -wave	
			[100]	$2m^1m^2m$	SD-SAM	
			[110]	$2m^2m^1m$	<i>d</i> -wave	
			[010]	$2m^1m^2m$	SD-SAM	
			[110]	$2m^2m^1m$	<i>d</i> -wave	

No.	Material entry	Index	Normals	Surface spin	Laue group	Surface character
21	$\text{Ba}_4\text{Ru}_3\text{O}_{10}$	0.692	[100] [010]	${}^2m^1m^2m$ ${}^2m^1m^2m$	SD-SAM SD-SAM	
22	$\text{Ba}_4\text{Ru}_3\text{O}_{10}$	0.693	[100] [010]	${}^2m^1m^2m$ ${}^2m^1m^2m$	SD-SAM SD-SAM	
23	Bi_2CuO_4	0.348	[1̄10] [110]	${}^2m^1m^2m$ ${}^2m^1m^2m$	SD-SAM SD-SAM	
24	Bi_2CuO_4	0.695	[1̄10] [110]	${}^2m^1m^2m$ ${}^2m^1m^2m$	SD-SAM SD-SAM	
25	Bi_2CuO_4	0.694	[1̄10] [110]	${}^2m^1m^2m$ ${}^2m^1m^2m$	SD-SAM SD-SAM	
26	$\text{CaCo}_{1.86}\text{As}_2$	0.691	[100] [1̄10] [010] [110]	${}^2m^1m^2m$ mmm ${}^2m^1m^2m$ mmm	SD-SAM AFM SD-SAM AFM	
27	CaCo_2P_2	1.252	[100] [1̄10] [010] [110]	${}^2m^1m^2m$ mmm ${}^2m^1m^2m$ mmm	SD-SAM AFM SD-SAM AFM	
28	$\text{CaCr}_{0.86}\text{Fe}_{3.14}\text{As}_3$	0.429	[010]	${}^2\mathbf{2/2m}$	d -wave	
29	CaFe_3O_5	1.756	[001] [100] [010]	${}^2/m$ ${}^2m^2m^1m$ $2/m$	AFM d -wave AFM	
30	CaFe_3O_5	1.762	[001] [100] [010]	${}^2/m$ ${}^2m^2m^1m$ $2/m$	AFM d -wave AFM	
31	CaMnBi_2	0.72	[001] [110] [110]	${}^24/1m^1m^2m$ ${}^2m^2m^1m$ ${}^2m^2m^1m$	d -wave d -wave d -wave	
32	CaMnGe	0.602	[001] [1̄10] [110]	${}^24/1m^1m^2m$ ${}^2m^2m^1m$ ${}^2m^2m^1m$	d -wave d -wave d -wave	
33	CaMn_2Ge_2	0.603	[001] [100] [1̄10] [010] [110]	${}^24/1m^1m^2m$ ${}^2m^1m^2m$ ${}^2m^2m^1m$ ${}^2m^1m^2m$ ${}^2m^2m^1m$	d -wave SD-SAM d -wave SD-SAM d -wave	
34	CaMn_2Ge_2	0.604	[001] [100] [1̄10] [010] [110]	${}^24/1m^1m^2m$ ${}^2m^1m^2m$ ${}^2m^2m^1m$ ${}^2m^1m^2m$ ${}^2m^2m^1m$	d -wave SD-SAM d -wave SD-SAM d -wave	

No.	Material entry	Index	Normals	Surface spin Laue group	Surface character
35	CaMnGe	0.601	[001] [1 $\bar{1}$ 0] [110]	$^{24/1}m^1m^2m$ $^2m^2m^1m$ $^2m^2m^1m$	<i>d</i> -wave <i>d</i> -wave <i>d</i> -wave
36	CaMn ₂ Sb ₂	0.523	[110] [100] [010]	$^22_z/2m_z$ $^22_z/2m_z$ $^22_z/2m_z$	SD-SAM SD-SAM SD-SAM
37	CaMn ₂ Sb ₂	0.92	[100]	$^22_z/2m_z$	SD-SAM
38	CaMnSi	0.599	[001] [1 $\bar{1}$ 0] [110]	$^{24/1}m^1m^2m$ $^2m^2m^1m$ $^2m^2m^1m$	<i>d</i> -wave <i>d</i> -wave <i>d</i> -wave
39	CaMnSi	0.600	[001] [1 $\bar{1}$ 0] [110]	$^{24/1}m^1m^2m$ $^2m^2m^1m$ $^2m^2m^1m$	<i>d</i> -wave <i>d</i> -wave <i>d</i> -wave
40	CaOFeS	1.472	[001] [110]	$^2/m$ $^22/2m$	AFM <i>d</i> -wave
41	CeCo ₂ P ₂	1.253	[100] [1 $\bar{1}$ 0] [010] [110]	$^2m^1m^2m$ mmm $^2m^1m^2m$ mmm	SD-SAM AFM SD-SAM AFM
42	CeCu ₂	0.290	[100] [010]	$^2m^1m^2m$ $^2m^1m^2m$	SD-SAM SD-SAM
43	CeMgPb	1.142	[001] [1 $\bar{1}$ 0] [110]	mmm mmm $^2m^1m^2m$	AFM AFM SD-SAM
44	CeMnAsO	0.186	[001] [1 $\bar{1}$ 0] [110]	$^{24/1}m^1m^2m$ $^2m^2m^1m$ $^2m^2m^1m$	<i>d</i> -wave <i>d</i> -wave <i>d</i> -wave
45	CeMnSbO	0.665	[001] [1 $\bar{1}$ 0] [110]	$^{24/1}m^1m^2m$ $^2m^2m^1m$ $^2m^2m^1m$	<i>d</i> -wave <i>d</i> -wave <i>d</i> -wave
46	CeMn ₂ Si ₂	1.488	[100] [1 $\bar{1}$ 0] [010] [110]	$^2m^1m^2m$ mmm $^2m^1m^2m$ mmm	SD-SAM AFM SD-SAM AFM
47	CeMn ₂ Si ₂	1.489	[100] [1 $\bar{1}$ 0] [010] [110]	$^2m^1m^2m$ mmm $^2m^1m^2m$ mmm	SD-SAM AFM SD-SAM AFM
48	CeMn ₂ Si ₂	1.490	[100] [1 $\bar{1}$ 0] [010] [110]	$^2m^1m^2m$ mmm $^2m^1m^2m$ mmm	SD-SAM AFM SD-SAM AFM

No.	Material entry	Index	Normals	Surface spin	Laue group	Surface character
49	Ce ₂ Ni ₃ Ge ₅	0.562	[001]	$^2m^2m^1m$	d -wave	
50	Ce ₂ Ni ₃ Ge ₅	0.563	[001] [100]	$^2m^1m^2m$ $^2m^1m^2m$	SD-SAM SD-SAM	
51	Ce ₃ Ni ₂ Ge ₇	1.413	[001] [100]	2mmm $^2m^1m^2m$	AFM SD-SAM	
52	CeNiGe ₃	1.414	[001] [010]	2mmm $^2m^1m^2m$	AFM SD-SAM	
53	Ce ₃ Ni ₂ Sn ₇	1.447	[001] [100]	2mmm $^2m^1m^2m$	AFM SD-SAM	
54	CeOs _{1.84} Ir _{0.16} Al ₁₀	1.148	[001] [100]	$^2/m$ $^2m^1m^2m$	AFM SD-SAM	
55	Ce ₂ PdGe ₃	0.166	[100] [110] [010] [110]	$^2m^1m^2m$ $^2m^2m^1m$ $^2m^1m^2m$ $^2m^2m^1m$	SD-SAM d -wave SD-SAM d -wave	
56	CeRh ₂ Si ₂	2.30	[001] [110]	2mmm $^2m^1m^2m$	AFM SD-SAM	
57	CeRu ₂ Al ₁₀	1.8	[001] [100]	$^2/m$ $^2m^1m^2m$	AFM SD-SAM	
58	CeScGe	1.376	[100] [110] [010] [110]	$^2m^1m^2m$ 2mmm $^2m^1m^2m$ 2mmm	SD-SAM AFM SD-SAM AFM	
59	CeScSi	1.378	[100] [110] [010] [110]	$^2m^1m^2m$ 2mmm $^2m^1m^2m$ 2mmm	SD-SAM AFM SD-SAM AFM	
60	Co ₄ Nb ₂ O ₉	0.111	[100]	$^22_z/2m_z$	SD-SAM	
61	Co ₃ O ₄	0.463	[110] [110] [101] [101] [011] [011]	$^2m^1m^2m$ $^2m^1m^2m$ $^2m^1m^2m$ $^2m^1m^2m$ $^2m^1m^2m$ $^2m^1m^2m$	SD-SAM SD-SAM SD-SAM SD-SAM SD-SAM SD-SAM	
62	CoRh ₂ O ₄	0.461	[110] [110] [101] [101] [011] [011]	$^2m^1m^2m$ $^2m^1m^2m$ $^2m^1m^2m$ $^2m^1m^2m$ $^2m^1m^2m$ $^2m^1m^2m$	SD-SAM SD-SAM SD-SAM SD-SAM SD-SAM SD-SAM	
63	CoSe ₂ O ₅	0.161	[001]	$^22/2m$	d -wave	

No.	Material entry	Index	Normals	Surface spin	Laue group	Surface character
					$^2\mathbf{2}/^2\mathbf{m}$	
64	Cr_2O_3	0.59	[110]	$^2\mathbf{2}_z/^2\mathbf{m}_z$	SD-SAM	d -wave
			[100]	$^2\mathbf{2}_z/^2\mathbf{m}_z$		
			[010]	$^2\mathbf{2}_z/^2\mathbf{m}_z$		
65	Cr_2O_3	0.110	[110]	$^2\mathbf{2}_z/^2\mathbf{m}_z$	SD-SAM	d -wave
			[100]	$^2\mathbf{2}_z/^2\mathbf{m}_z$		
			[010]	$^2\mathbf{2}_z/^2\mathbf{m}_z$		
66	Cr_2TeO_6	0.959	[100]	$^2\mathbf{2}/^2\mathbf{m}$	SD-SAM	d -wave
			[1\bar{1}0]	$^2\mathbf{m}^1\mathbf{m}^2\mathbf{m}$		
			[010]	$^2\mathbf{2}/^2\mathbf{m}$		
			[110]	$^2\mathbf{m}^1\mathbf{m}^2\mathbf{m}$		
67	Cr_2TeO_6	0.76	[100]	$^2\mathbf{2}/^2\mathbf{m}$	SD-SAM	d -wave
			[1\bar{1}0]	$^2\mathbf{m}^1\mathbf{m}^2\mathbf{m}$		
			[010]	$^2\mathbf{2}/^2\mathbf{m}$		
			[110]	$^2\mathbf{m}^1\mathbf{m}^2\mathbf{m}$		
68	Cr_2TeO_6	0.143	[100]	$^2\mathbf{2}/^2\mathbf{m}$	SD-SAM	d -wave
			[1\bar{1}0]	$^2\mathbf{m}^1\mathbf{m}^2\mathbf{m}$		
			[010]	$^2\mathbf{2}/^2\mathbf{m}$		
			[110]	$^2\mathbf{m}^1\mathbf{m}^2\mathbf{m}$		
69	Cr_2WO_6	0.75	[100]	$^2\mathbf{2}/^2\mathbf{m}$	SD-SAM	d -wave
			[1\bar{1}0]	$^2\mathbf{m}^1\mathbf{m}^2\mathbf{m}$		
			[010]	$^2\mathbf{2}/^2\mathbf{m}$		
			[110]	$^2\mathbf{m}^1\mathbf{m}^2\mathbf{m}$		
70	Cr_2WO_6	0.144	[100]	$^2\mathbf{2}/^2\mathbf{m}$	SD-SAM	d -wave
			[1\bar{1}0]	$^2\mathbf{m}^1\mathbf{m}^2\mathbf{m}$		
			[010]	$^2\mathbf{2}/^2\mathbf{m}$		
			[110]	$^2\mathbf{m}^1\mathbf{m}^2\mathbf{m}$		
71	CsCo_2Se_2	1.458	[100]	$^2\mathbf{m}^1\mathbf{m}^2\mathbf{m}$	SD-SAM	AFM
			[1\bar{1}0]	mmm		
			[010]	$^2\mathbf{m}^1\mathbf{m}^2\mathbf{m}$		
			[110]	mmm		
72	$\text{Cs}_2\text{FeCl}_5\text{D}_2\text{O}$	0.252	[010]	$^2\mathbf{2}_z/^2\mathbf{m}_z$	SD-SAM	
73	$\text{Cs}_2[\text{FeCl}_5(\text{H}_2\text{O})]$	0.476	[010]	$^2\mathbf{2}_z/^2\mathbf{m}_z$	SD-SAM	
74	CsFeO_2	0.457	[010]	$^2\mathbf{2}/^2\mathbf{m}$	d -wave	
75	CsMnBi	1.546	[001]	$^2\mathbf{4}/^1\mathbf{m}^1\mathbf{m}^2\mathbf{m}$	AFM	d -wave
			[100]	$2/m$		
			[1\bar{1}0]	mmm		
			[010]	$2/m$		
			[110]	mmm		
76	CsMnP	1.548	[001]	$^2\mathbf{4}/^1\mathbf{m}^1\mathbf{m}^2\mathbf{m}$	AFM	d -wave
			[100]	$2/m$		
			[1\bar{1}0]	mmm		
			[010]	$2/m$		

No.	Material entry	Index	Normals	Surface spin	Laue group	Surface character
					[110]	
77	CsMnP	1.547	[001]	$^24/1m^1m^2m$	<i>d</i> -wave	
			[100]	$2/m$	AFM	
			[110]	mmm	AFM	
			[010]	$2/m$	AFM	
			[110]	mmm	AFM	
78	$\text{CuBr}(\text{C}_4\text{H}_4\text{N}_2)_2(\text{BF}_4)$	1.473	[001]	$^14/1m^2m^2m$	<i>g</i> -wave	
			[100]	$2/m$	AFM	
			[110]	mmm	AFM	
			[010]	$2/m$	AFM	
			[110]	mmm	AFM	
79	$\text{CuCl}(\text{C}_4\text{H}_4\text{N}_2)_2(\text{BF}_4)$	1.474	[001]	$^14/1m^2m^2m$	<i>g</i> -wave	
			[100]	$2/m$	AFM	
			[110]	mmm	AFM	
			[010]	$2/m$	AFM	
			[110]	mmm	AFM	
80	$\text{Cu}_3\text{Co}_2\text{SbO}_6$	1.258	[010]	$^22_z/2m_z$	SD-SAM	
81	CuMnAs	0.222	[110]	$^2m^1m^2m$	SD-SAM	
			[110]	$^2m^1m^2m$	SD-SAM	
82	$\text{Cu}_{0.95}\text{MnAs}$	0.223	[010]	$^22/2m$	<i>d</i> -wave	
83	CuMnAs	0.881	[110]	$^2m^1m^2m$	SD-SAM	
			[110]	$^2m^1m^2m$	SD-SAM	
84	$\text{Cu}_3\text{Ni}_2\text{SbO}_6$	1.259	[010]	$^22_z/2m_z$	SD-SAM	
85	DyB_4	0.22	[001]	$^2m^1m^2m$	SD-SAM	
86	DyCoSi_2	0.453	[100]	$^2m^1m^2m$	SD-SAM	
87	$\text{DyGe}_{1.75}$	0.341	[001]	$^2m^1m^2m$	SD-SAM	
			[100]	$^2m^1m^2m$	SD-SAM	
88	DyMn_2Ge_2	1.693	[100]	$^2m^1m^2m$	SD-SAM	
			[110]	mmm	AFM	
			[010]	$^2m^1m^2m$	SD-SAM	
			[110]	mmm	AFM	
89	DyNiAl_4	1.475	[001]	$2/m$	AFM	
			[100]	$^2m^1m^2m$	SD-SAM	
90	DyVO_4	1.664	[010]	$^2m^1m^2m$	SD-SAM	
91	ErB_4	0.468	[001]	$^2m^1m^2m$	SD-SAM	
92	Er_2CoGa_8	1.222	[001]	mmm	AFM	
			[100]	mmm	AFM	
			[010]	$^2m^1m^2m$	SD-SAM	

No.	Material entry	Index	Normals	Surface spin	Laue group	Surface character
93	ErCr ₂ Si ₂	0.486	[001]	$^{24/1}m^1m^2m$	<i>d</i> -wave	
			[100]	$^2m^1m^2m$	SD-SAM	
			[110]	$^2m^2m^1m$	<i>d</i> -wave	
			[010]	$^2m^1m^2m$	SD-SAM	
			[110]	$^2m^2m^1m$	<i>d</i> -wave	
94	ErFe ₆ Ge ₆	1.632	[010]	$^2m^1m^2m$	SD-SAM	
			[001]	$^2m^1m^2m$	SD-SAM	
95	ErGe ₃	0.330	[100]	$^2m^1m^2m$	SD-SAM	
96	ErMn ₂ Ge ₂	1.638	[100]	$^2m^1m^2m$	SD-SAM	
			[110]	mmm	AFM	
			[010]	$^2m^1m^2m$	SD-SAM	
			[110]	mmm	AFM	
97	ErMn ₂ Ge ₂	1.640	[100]	$^2m^1m^2m$	SD-SAM	
			[110]	mmm	AFM	
			[010]	$^2m^1m^2m$	SD-SAM	
			[110]	mmm	AFM	
98	ErMn ₂ Ge ₂	1.639	[100]	$^2m^1m^2m$	SD-SAM	
			[110]	mmm	AFM	
			[010]	$^2m^1m^2m$	SD-SAM	
			[110]	mmm	AFM	
99	ErMn ₂ Si ₂	1.636	[100]	$^2m^1m^2m$	SD-SAM	
			[110]	mmm	AFM	
			[010]	$^2m^1m^2m$	SD-SAM	
			[110]	mmm	AFM	
100	ErMn ₂ Si ₂	1.637	[100]	$^2m^1m^2m$	SD-SAM	
			[110]	mmm	AFM	
			[010]	$^2m^1m^2m$	SD-SAM	
			[110]	mmm	AFM	
101	Er ₂ PtGe ₆	0.932	[100]	$^2m^1m^2m$	SD-SAM	
			[010]	$^2m^1m^2m$	SD-SAM	
102	Er ₂ PtGe ₆	0.909	[100]	$^2m^1m^2m$	SD-SAM	
			[010]	$^2m^1m^2m$	SD-SAM	
103	EuMnBi ₂	2.50	[100]	$^2m^1m^2m$	SD-SAM	
			[110]	$^2m^2m^1m$	<i>d</i> -wave	
			[010]	$^2m^1m^2m$	SD-SAM	
			[110]	$^2m^2m^1m$	<i>d</i> -wave	
104	EuMnBi ₂	0.919	[001]	$^{24/1}m^1m^2m$	<i>d</i> -wave	
			[100]	$^2m^1m^2m$	SD-SAM	
			[110]	$^2m^2m^1m$	<i>d</i> -wave	
			[010]	$^2m^1m^2m$	SD-SAM	
			[110]	$^2m^2m^1m$	<i>d</i> -wave	
105	EuMnBi ₂	2.98	[100]	$^2m^1m^2m$	SD-SAM	
			[010]	$^2m^1m^2m$	SD-SAM	

No.	Material entry	Index	Normals	Surface spin	Laue group	Surface character
106	EuMnBi ₂	0.426	[001]	$^24/1m^1m^2m$	<i>d</i> -wave	
			[100]	$^2m^1m^2m$	SD-SAM	
			[1 $\bar{1}$ 0]	$^2m^2m^1m$	<i>d</i> -wave	
			[010]	$^2m^1m^2m$	SD-SAM	
			[110]	$^2m^2m^1m$	<i>d</i> -wave	
107	EuMn ₂ Ge ₂	0.474	[001]	$^24/1m^1m^2m$	<i>d</i> -wave	
			[100]	$^2m^1m^2m$	SD-SAM	
			[1 $\bar{1}$ 0]	$^2m^2m^1m$	<i>d</i> -wave	
			[010]	$^2m^1m^2m$	SD-SAM	
			[110]	$^2m^2m^1m$	<i>d</i> -wave	
108	EuMn ₂ Si ₂	1.453	[100]	$^2m^1m^2m$	SD-SAM	
			[1 $\bar{1}$ 0]	mmm	AFM	
			[010]	$^2m^1m^2m$	SD-SAM	
			[110]	mmm	AFM	
109	EuTiO ₃	0.16	[001]	$^24/1m^1m^2m$	<i>d</i> -wave	
			[100]	$^2m^2m^1m$	<i>d</i> -wave	
			[1 $\bar{1}$ 0]	$^2m^1m^2m$	SD-SAM	
			[010]	$^2m^2m^1m$	<i>d</i> -wave	
			[110]	$^2m^1m^2m$	SD-SAM	
110	EuZrO ₃	0.146	[010]	$^22/2m$	<i>d</i> -wave	
111	EuZrO ₃	0.147	[010]	$^22/2m$	<i>d</i> -wave	
112	Fe ₃ BO ₅	0.386	[001]	$^22/2m$	<i>d</i> -wave	
113	FeGe ₂	1.557	[001]	$^14/1m^2m^2m$	<i>g</i> -wave	
			[1 $\bar{1}$ 0]	mmm	AFM	
			[110]	mmm	AFM	
114	Fe ₂ MnBO ₅	1.391	[001]	$^2m^2m^1m$	<i>d</i> -wave	
			[100]	$2/m$	AFM	
			[010]	$2/m$	AFM	
115	Fe ₄ Nb ₂ O ₉	0.442	[010]	$^22_z/2m_z$	SD-SAM	
116	Fe ₄ Nb ₂ O ₉	0.443	[110]	$^22_z/2m_z$	SD-SAM	
			[100]	$^22_z/2m_z$	SD-SAM	
			[010]	$^22_z/2m_z$	SD-SAM	
117	Fe _{0.35} NbS ₂	1.677	[100]	$^22_z/2m_z$	SD-SAM	
			[010]	$\bar{1}$	AFM	
			[001]	$\bar{1}$	AFM	
118	Fe _{0.967} Nb ₃ S ₆	1.589	[001]	$\bar{1}$	AFM	
			[100]	$^22_z/2m_z$	SD-SAM	
			[010]	$\bar{1}$	AFM	
119	FeSn ₂	1.556	[001]	$^14/1m^2m^2m$	<i>g</i> -wave	
			[1 $\bar{1}$ 0]	mmm	AFM	
			[110]	mmm	AFM	

No.	Material entry	Index	Normals	Surface spin	Laue group	Surface character
120	Fe_2TeO_6	0.142	[100]	$^2\cancel{2}/^2m$	d -wave	
			[110]	$^2m^1m^2m$	SD-SAM	
			[010]	$^2\cancel{2}/^2m$	d -wave	
			[110]	$^2m^1m^2m$	SD-SAM	
121	Fe_2TeO_6	0.960	[100]	$^2\cancel{2}/^2m$	d -wave	
			[110]	$^2m^1m^2m$	SD-SAM	
			[010]	$^2\cancel{2}/^2m$	d -wave	
			[110]	$^2m^1m^2m$	SD-SAM	
122	Fe_2WO_6	0.814	[100]	$^2\cancel{2}/^2m$	d -wave	
123	GdAlO_3	0.410	[001]	$^2\cancel{2}/^2m$	d -wave	
124	GdNiSi_3	0.406	[001]	$^2m^1m^2m$	SD-SAM	
			[100]	$^2m^1m^2m$	SD-SAM	
125	GdVO_4	0.198	[100]	$^2m^1m^2m$	SD-SAM	
			[010]	$^2m^1m^2m$	SD-SAM	
126	HoCr_2Si_2	0.519	[001]	$^2\cancel{4}/^1m^1m^2m$	d -wave	
			[100]	$^2m^1m^2m$	SD-SAM	
			[110]	$^2\cancel{m}^2m^1m$	d -wave	
			[010]	$^2m^1m^2m$	SD-SAM	
			[110]	$^2\cancel{m}^2m^1m$	d -wave	
127	HoCr_2Si_2	0.465	[001]	$^2\cancel{4}/^1m^1m^2m$	d -wave	
			[100]	$^2m^1m^2m$	SD-SAM	
			[110]	$^2\cancel{m}^2m^1m$	d -wave	
			[010]	$^2m^1m^2m$	SD-SAM	
			[110]	$^2\cancel{m}^2m^1m$	d -wave	
128	Ho_3Ge_4	1.356	[001]	$^2/m$	AFM	
			[100]	$^2m^1m^2m$	SD-SAM	
			[010]	$^2m^1m^2m$	SD-SAM	
129	HoMnO_3	1.20	[001]	$^2/m$	AFM	
			[100]	$^2\cancel{2}/^2m$	d -wave	
			[010]	$\bar{1}$	AFM	
130	$\text{HoNi}_{0.64}\text{Ge}_2$	0.567	[100]	$^2m^1m^2m$	SD-SAM	
131	HoNiSi_2	1.696	[001]	$^2/m$	AFM	
			[100]	$^2m^1m^2m$	SD-SAM	
132	$\text{Ho}_2\text{O}_2\text{Se}$	1.213	[100]	$^22_z/^2m_z$	SD-SAM	
133	Ho_2RhIn_8	1.139	[001]	mmm	AFM	
			[100]	$^2m^1m^2m$	SD-SAM	
			[010]	mmm	AFM	
134	$\text{K}_2\text{CoP}_2\text{O}_7$	0.230	[001]	$^2\cancel{m}^2m^1m$	d -wave	
			[100]	$^2\cancel{2}/^2m$	d -wave	
			[110]	$^2\cancel{m}^2m^1m$	d -wave	
			[010]	$^2\cancel{2}/^2m$	d -wave	

No.	Material entry	Index	Normals	Surface	Laue group	Surface character
				[110]	$^2m^2m^1m$	
135	KCuMnS ₂	1.392	[001]	<i>mmm</i>	AFM	
			[110]	$^2m^2m^1m$	<i>d</i> -wave	
			[110]	<i>mmm</i>	AFM	
136	KFeO ₂	0.460	[010]	$^22/2m$	<i>d</i> -wave	
137	KFeO ₂	0.459	[010]	$^22/2m$	<i>d</i> -wave	
138	KMnAs	1.554	[001]	$^24/1m^1m^2m$	<i>d</i> -wave	
			[100]	$2/m$	AFM	
			[110]	<i>mmm</i>	AFM	
			[010]	$2/m$	AFM	
			[110]	<i>mmm</i>	AFM	
139	KMnAs	1.553	[001]	$^24/1m^1m^2m$	<i>d</i> -wave	
			[100]	$2/m$	AFM	
			[110]	<i>mmm</i>	AFM	
			[010]	$2/m$	AFM	
			[110]	<i>mmm</i>	AFM	
140	KMnBi	0.618	[001]	$^24/1m^1m^2m$	<i>d</i> -wave	
			[110]	$^2m^2m^1m$	<i>d</i> -wave	
			[110]	$^2m^2m^1m$	<i>d</i> -wave	
141	KMnP	1.540	[001]	$^24/1m^1m^2m$	<i>d</i> -wave	
			[100]	$2/m$	AFM	
			[110]	<i>mmm</i>	AFM	
			[010]	$2/m$	AFM	
			[110]	<i>mmm</i>	AFM	
142	KMnP	1.539	[001]	$^24/1m^1m^2m$	<i>d</i> -wave	
			[100]	$2/m$	AFM	
			[110]	<i>mmm</i>	AFM	
			[010]	$2/m$	AFM	
			[110]	<i>mmm</i>	AFM	
143	KMnSb	0.617	[001]	$^24/1m^1m^2m$	<i>d</i> -wave	
			[110]	$^2m^2m^1m$	<i>d</i> -wave	
			[110]	$^2m^2m^1m$	<i>d</i> -wave	
144	KTb ₃ F ₁₂	1.59	[001]	$^24/1m$	<i>d</i> -wave	
145	La ₂ CoO ₄	1.403	[001]	$2/m$	AFM	
			[010]	$^2m^1m^2m$	SD-SAM	
146	LaCrAsO	1.146	[001]	$^24/1m^1m^2m$	<i>d</i> -wave	
			[100]	$2/m$	AFM	
			[110]	<i>mmm</i>	AFM	
			[010]	$2/m$	AFM	
			[110]	<i>mmm</i>	AFM	
147	La ₂ CuO ₄	1.405	[010]	$2/m$	AFM	
			[001]	$^2m^1m^2m$	SD-SAM	

No.	Material entry	Index	Normals	Surface spin	Laue group	Surface character
148	La ₂ CuO ₄	1.23	[001] [010]	$2/m$ $2m^1m^2m$	AFM SD-SAM	
149	La(Fe _{0.91} Al _{0.09}) ₁₃	1.621	[100]	mmm	AFM	
			[110]	$2m^1m^2m$	SD-SAM	
			[010]	mmm	AFM	
			[110]	$2m^1m^2m$	SD-SAM	
150	LaMnAsO	0.619	[001] [110] [110]	$24/1m^1m^2m$ $2m^2m^1m$ $2m^2m^1m$	<i>d</i> -wave <i>d</i> -wave <i>d</i> -wave	
151	LaMnAsO	0.624	[001] [110] [110]	$24/1m^1m^2m$ $2m^2m^1m$ $2m^2m^1m$	<i>d</i> -wave <i>d</i> -wave <i>d</i> -wave	
152	LaMnSbO	0.667	[001] [110] [110]	$24/1m^1m^2m$ $2m^2m^1m$ $2m^2m^1m$	<i>d</i> -wave <i>d</i> -wave <i>d</i> -wave	
153	LaMn ₂ Si ₂	0.472	[001]	$24/1m^1m^2m$	<i>d</i> -wave	
			[100]	$2m^1m^2m$	SD-SAM	
			[110]	$2m^2m^1m$	<i>d</i> -wave	
			[010]	$2m^1m^2m$	SD-SAM	
			[110]	$2m^2m^1m$	<i>d</i> -wave	
154	LaMn ₂ Si ₂	0.498	[001]	$24/1m^1m^2m$	<i>d</i> -wave	
			[100]	$2m^1m^2m$	SD-SAM	
			[110]	$2m^2m^1m$	<i>d</i> -wave	
			[010]	$2m^1m^2m$	SD-SAM	
			[110]	$2m^2m^1m$	<i>d</i> -wave	
155	La ₂ NiO ₄	1.42	[010] [001]	$2/m$ $2m^1m^2m$	AFM SD-SAM	
156	La ₂ NiO ₃ F ₂	1.388	[001] [100]	$2/m$ $2m^1m^2m$	AFM SD-SAM	
157	LaSr ₃ Fe ₃ O ₉	1.481	[001] [100]	$2/m$ $2m^1m^2m$	AFM SD-SAM	
158	Li ₂ Co(SO ₄) ₂	0.244	[010]	$22/2m$	<i>d</i> -wave	
159	LiFe(SO ₄) ₂	0.246	[010]	$22/2m$	<i>d</i> -wave	
160	Li _{1.5} Fe(SO ₄) ₂	0.245	[010]	$22/2m$	<i>d</i> -wave	
161	Li ₂ Fe(SO ₄) ₂	0.243	[010]	$22/2m$	<i>d</i> -wave	
162	LiMnAs	1.550	[001]	$24/1m^1m^2m$	<i>d</i> -wave	
			[100]	$2/m$	AFM	
			[110]	mmm	AFM	
			[010]	$2/m$	AFM	
			[110]	mmm	AFM	

No.	Material entry	Index	Normals	Surface spin	Laue group	Surface character
163	LiMnAs	1.552	[001]	$^{24/1}m^1m^2m$	<i>d</i> -wave	
			[100]	$2/m$	AFM	
			[110]	mmm	AFM	
			[010]	$2/m$	AFM	
			[110]	mmm	AFM	
164	LiMnAs	1.551	[001]	$^{24/1}m^1m^2m$	<i>d</i> -wave	
			[100]	$2/m$	AFM	
			[110]	mmm	AFM	
			[010]	$2/m$	AFM	
			[110]	mmm	AFM	
165	Li ₂ Ni(SO ₄) ₂	0.71	[010]	$^{22/2}m$	<i>d</i> -wave	
166	Li ₂ VOSiO ₄	1.9	[001]	$^{2}m^1m^2m$	AFM	
			[110]	$^{2}m^1m^2m$	SD-SAM	
167	LuMn ₂ Ge ₂	1.689	[100]	$^{2}m^1m^2m$	SD-SAM	
			[110]	mmm	AFM	
			[010]	$^{2}m^1m^2m$	SD-SAM	
			[110]	mmm	AFM	
168	LuMnO ₃	1.101	[100]	$2/m$	AFM	
			[010]	$^{22/2}m$	<i>d</i> -wave	
			[001]	$\bar{1}$	AFM	
169	MnAl ₂ O ₄	0.462	[110]	$^{2}m^1m^2m$	SD-SAM	
			[110]	$^{2}m^1m^2m$	SD-SAM	
			[101]	$^{2}m^1m^2m$	SD-SAM	
			[101]	$^{2}m^1m^2m$	SD-SAM	
			[011]	$^{2}m^1m^2m$	SD-SAM	
			[011]	$^{2}m^1m^2m$	SD-SAM	
			[101]	$^{2}m^1m^2m$	SD-SAM	
170	Mn ₂ Au	0.640	[100]	$^{2}m^1m^2m$	SD-SAM	
			[110]	$^{2}m^1m^2m$	SD-SAM	
			[010]	$^{2}m^1m^2m$	SD-SAM	
			[110]	$^{2}m^1m^2m$	SD-SAM	
171	Mn ₂ Au	0.639	[100]	$^{2}m^1m^2m$	SD-SAM	
			[110]	$^{2}m^1m^2m$	SD-SAM	
			[010]	$^{2}m^1m^2m$	SD-SAM	
			[110]	$^{2}m^1m^2m$	SD-SAM	
172	MnCl ₂ (CO(NH ₂) ₂) ₂	1.659	[100]	$^{22/2}m$	<i>d</i> -wave	
			[010]	$^{22/2}m$	<i>d</i> -wave	
173	MnNb ₂ O ₆	0.815	[001]	$^{22/2}m$	<i>d</i> -wave	
			[100]	$^{22/2}m$	<i>d</i> -wave	
174	Mn ₄ Nb ₂ O ₉	0.507	[110]	$^{2}2_z/2m_z$	SD-SAM	
			[100]	$^{2}2_z/2m_z$	SD-SAM	
			[010]	$^{2}2_z/2m_z$	SD-SAM	
175	Mn ₆ Ni ₁₆ Si ₇	1.454	[001]	$^{24/1}m^1m^2m$	<i>d</i> -wave	
			[100]	mmm	AFM	
			[110]	$^{2}m^1m^2m$	SD-SAM	
			[110]	$^{2}m^1m^2m$	SD-SAM	

No.	Material entry	Index	Normals	Surface spin	Laue group	Surface character
			[010] [110]	mmm $2m^1m^2m$	AFM SD-SAM	
176	Mn ₃ O ₄	1.1	[001] [100] [010]	$2/m$ $2m^1m^2m$ $2/m$	AFM SD-SAM AFM	
177	Mn ₃ Pt	1.143	[001] [100] [110] [010] [110]	$24/1m^1m^2m$ mmm mmm mmm mmm	d -wave AFM AFM AFM AFM	
178	MnS ₂	1.18	[001] [100] [010]	$\bar{1}$ $2/m$ $22/2m$	AFM AFM d -wave	
179	Mn ₄ Ta ₂ O ₉	0.526	[110] [100] [010]	$22_z/2m_z$ $22_z/2m_z$ $22_z/2m_z$	SD-SAM SD-SAM SD-SAM	
180	Mn ₄ Ta ₂ O ₉	0.477	[110] [100] [010]	$22_z/2m_z$ $22_z/2m_z$ $22_z/2m_z$	SD-SAM SD-SAM SD-SAM	
181	MnTa ₂ O ₆	0.816	[001] [100]	$22/2m$ $22/2m$	d -wave d -wave	
182	MoP ₃ SiO ₁₁	0.804	[110] [100] [010]	$22_z/2m_z$ $22_z/2m_z$ $22_z/2m_z$	SD-SAM SD-SAM SD-SAM	
183	MoP ₃ SiO ₁₁	0.728	[110] [100] [010]	$22_z/2m_z$ $22_z/2m_z$ $22_z/2m_z$	SD-SAM SD-SAM SD-SAM	
184	NaCeO ₂	0.525	[100] [010]	$2m^1m^2m$ $2m^1m^2m$	SD-SAM SD-SAM	
185	Na ₂ Co ₂ TeO ₆	1.184	[001] [010]	$\bar{1}$ $22_z/2m_z$	AFM SD-SAM	
186	NaFeSO ₄ F	1.121	[010]	$22_z/2m_z$	SD-SAM	
187	NaMnAs	0.629	[001] [110] [110]	$24/1m^1m^2m$ $2m^2m^1m$ $2m^2m^1m$	d -wave d -wave d -wave	
188	NaMnAs	0.630	[001] [110] [110]	$24/1m^1m^2m$ $2m^2m^1m$ $2m^2m^1m$	d -wave d -wave d -wave	
189	NaMnBi	0.635	[001] [110] [110]	$24/1m^1m^2m$ $2m^2m^1m$ $2m^2m^1m$	d -wave d -wave d -wave	

No.	Material entry	Index	Normals	Surface spin Laue group	Surface character
190	NaMnBi	0.634	[001] [1 $\bar{1}$ 0] [110]	$^{24/1}m^1m^2m$ $^2m^2m^1m$ $^2m^2m^1m$	<i>d</i> -wave <i>d</i> -wave <i>d</i> -wave
191	NaMnP	0.628	[001] [1 $\bar{1}$ 0] [110]	$^{24/1}m^1m^2m$ $^2m^2m^1m$ $^2m^2m^1m$	<i>d</i> -wave <i>d</i> -wave <i>d</i> -wave
192	NaMnP	0.627	[001] [1 $\bar{1}$ 0] [110]	$^{24/1}m^1m^2m$ $^2m^2m^1m$ $^2m^2m^1m$	<i>d</i> -wave <i>d</i> -wave <i>d</i> -wave
193	NaMnP	0.626	[001] [1 $\bar{1}$ 0] [110]	$^{24/1}m^1m^2m$ $^2m^2m^1m$ $^2m^2m^1m$	<i>d</i> -wave <i>d</i> -wave <i>d</i> -wave
194	NaMnSb	0.632	[001] [1 $\bar{1}$ 0] [110]	$^{24/1}m^1m^2m$ $^2m^2m^1m$ $^2m^2m^1m$	<i>d</i> -wave <i>d</i> -wave <i>d</i> -wave
195	NaMnSb	0.631	[001] [1 $\bar{1}$ 0] [110]	$^{24/1}m^1m^2m$ $^2m^2m^1m$ $^2m^2m^1m$	<i>d</i> -wave <i>d</i> -wave <i>d</i> -wave
196	NdCu ₂	1.620	[010]	$^2m^1m^2m$	SD-SAM
197	Nd ₆ Fe ₁₃ Sn	1.451	[100] [1 $\bar{1}$ 0] [010] [110]	$^2m^1m^2m$ mmm $^2m^1m^2m$ mmm	SD-SAM AFM SD-SAM AFM
198	NdMgPb	1.141	[100] [1 $\bar{1}$ 0] [010] [110]	$^2m^1m^2m$ mmm $^2m^1m^2m$ mmm	SD-SAM AFM SD-SAM AFM
199	NdMnAsO	0.623	[001] [1 $\bar{1}$ 0] [110]	$^{24/1}m^1m^2m$ $^2m^2m^1m$ $^2m^2m^1m$	<i>d</i> -wave <i>d</i> -wave <i>d</i> -wave
200	NdMnAsO	0.620	[001] [1 $\bar{1}$ 0] [110]	$^{24/1}m^1m^2m$ $^2m^2m^1m$ $^2m^2m^1m$	<i>d</i> -wave <i>d</i> -wave <i>d</i> -wave
201	NdMn ₂ Si ₂	1.494	[100] [1 $\bar{1}$ 0] [010] [110]	$^2m^1m^2m$ mmm $^2m^1m^2m$ mmm	SD-SAM AFM SD-SAM AFM
202	NdMn ₂ Si ₂	1.493	[100] [1 $\bar{1}$ 0] [010] [110]	$^2m^1m^2m$ mmm $^2m^1m^2m$ mmm	SD-SAM AFM SD-SAM AFM
203	NdNiMg ₁₅	1.457	[001] [1 $\bar{1}$ 0]	mmm $^2m^1m^2m$	AFM SD-SAM

No.	Material entry	Index	Normals	Surface spin	Laue group	Surface character
204	Nd ₂ NiO ₄	1.371	[010] [001]	$2/m$ $2m^1m^2m$	AFM SD-SAM	
205	NdScSiC _{0.5} H _{0.2}	1.503	[100]	$2m^1m^2m$	SD-SAM	
			[110]	mmm	AFM	
			[010]	$2m^1m^2m$	SD-SAM	
			[110]	mmm	AFM	
206	Ni _{1.64} Co _{0.36} Mn _{1.28} Ga _{0.72}	1.198	[001]	$24/1m^1m^2m$	<i>d</i> -wave	
			[110]	mmm	AFM	
			[110]	mmm	AFM	
207	NpCo ₂	0.126	[110]	$2m^1m^2m$	SD-SAM	
			[110]	$2m^1m^2m$	SD-SAM	
			[101]	$2m^1m^2m$	SD-SAM	
			[101]	$2m^1m^2m$	SD-SAM	
			[011]	$2m^1m^2m$	SD-SAM	
			[011]	$2m^1m^2m$	SD-SAM	
208	Pb ₅ Fe ₃ TiO ₁₁ Cl	0.435	[001]	$4/mmm$	AFM	
			[100]	mmm	AFM	
			[110]	$2m^1m^2m$	SD-SAM	
			[010]	mmm	AFM	
			[110]	$2m^1m^2m$	SD-SAM	
209	PrFeAsO	1.586	[001] [010]	$2/m$ $22/2m$	AFM <i>d</i> -wave	
210	PrFeAsO	1.585	[001] [010]	mmm $2m^2m^1m$	AFM <i>d</i> -wave	
211	Pr ₆ Fe ₁₃ Sn	1.450	[010] [100]	$22/2m$ $22_z/2m_z$	<i>d</i> -wave SD-SAM	
212	PrMgPb	1.140	[100]	$2m^1m^2m$	SD-SAM	
			[110]	mmm	AFM	
			[010]	$2m^1m^2m$	SD-SAM	
			[110]	mmm	AFM	
213	PrMnSi ₂	1.628	[001] [100]	$2/m$ $2m^1m^2m$	AFM SD-SAM	
214	PrMn ₂ Si ₂	1.492	[100]	$2m^1m^2m$	SD-SAM	
			[110]	mmm	AFM	
			[010]	$2m^1m^2m$	SD-SAM	
			[110]	mmm	AFM	
215	PrMn ₂ Si ₂	1.491	[100]	$2m^1m^2m$	SD-SAM	
			[110]	mmm	AFM	
			[010]	$2m^1m^2m$	SD-SAM	
			[110]	mmm	AFM	
216	Pr ₂ Pd ₂ In	1.334	[001]	$2m^1m^2m$	SD-SAM	
			[100]	$2/m$	AFM	
			[010]	$2/m$	AFM	

No.	Material entry	Index	Normals	Surface spin	Laue group	Surface character
217	RbFeO ₂	0.455	[010]	$^2\mathbf{2}/^2\mathbf{m}$	<i>d</i> -wave	
218	RbMnAs	1.544	[001]	$^2\mathbf{4}/^1\mathbf{m}^1\mathbf{m}^2\mathbf{m}$	<i>d</i> -wave	
			[100]	$2/m$	AFM	
			[110]	mmm	AFM	
			[010]	$2/m$	AFM	
			[110]	mmm	AFM	
219	RbMnAs	1.543	[001]	$^2\mathbf{4}/^1\mathbf{m}^1\mathbf{m}^2\mathbf{m}$	<i>d</i> -wave	
			[100]	$2/m$	AFM	
			[110]	mmm	AFM	
			[010]	$2/m$	AFM	
			[110]	mmm	AFM	
220	RbMnBi	1.545	[001]	$^2\mathbf{4}/^1\mathbf{m}^1\mathbf{m}^2\mathbf{m}$	<i>d</i> -wave	
			[100]	$2/m$	AFM	
			[110]	mmm	AFM	
			[010]	$2/m$	AFM	
			[110]	mmm	AFM	
221	RbMnP	1.542	[001]	$^2\mathbf{4}/^1\mathbf{m}^1\mathbf{m}^2\mathbf{m}$	<i>d</i> -wave	
			[100]	$2/m$	AFM	
			[110]	mmm	AFM	
			[010]	$2/m$	AFM	
			[110]	mmm	AFM	
222	RbMnP	1.541	[001]	$^2\mathbf{4}/^1\mathbf{m}^1\mathbf{m}^2\mathbf{m}$	<i>d</i> -wave	
			[100]	$2/m$	AFM	
			[110]	mmm	AFM	
			[010]	$2/m$	AFM	
			[110]	mmm	AFM	
223	RuCl ₃	1.228	[010]	$^2\mathbf{2}_z/^2\mathbf{m}_z$	SD-SAM	
224	Sr ₂ Co ₂ O ₅	0.799	[100]	$^2\mathbf{2}/^2\mathbf{m}$	<i>d</i> -wave	
225	Sr ₂ CoO ₃ Cl	1.389	[001] [010]	$^2\mathbf{m}^1\mathbf{m}^2\mathbf{m}$ $^2\mathbf{m}^1\mathbf{m}^2\mathbf{m}$	AFM SD-SAM	
226	SrCo ₂ V ₂ O ₈	1.71	[001] [010]	$^2\mathbf{m}^1\mathbf{m}^2\mathbf{m}$ $^2\mathbf{2}/^2\mathbf{m}$	SD-SAM <i>d</i> -wave	
227	SrCr ₂ As ₂	0.364	[001]	$^2\mathbf{4}/^1\mathbf{m}^1\mathbf{m}^2\mathbf{m}$	<i>d</i> -wave	
			[100]	$^2\mathbf{m}^1\mathbf{m}^2\mathbf{m}$	SD-SAM	
			[110]	$^2\mathbf{m}^2\mathbf{m}^1\mathbf{m}$	<i>d</i> -wave	
			[010]	$^2\mathbf{m}^1\mathbf{m}^2\mathbf{m}$	SD-SAM	
			[110]	$^2\mathbf{m}^2\mathbf{m}^1\mathbf{m}$	<i>d</i> -wave	
228	Sr ₂ Cr ₃ As ₂ O ₂	1.461	[001]	$^2\mathbf{4}/^1\mathbf{m}^1\mathbf{m}^2\mathbf{m}$	<i>d</i> -wave	
			[110]	mmm	AFM	
			[110]	mmm	AFM	
229	Sr ₂ Fe _{1.9} Co _{0.1} O _{5.5}	0.400	[001]	$^2\mathbf{m}^1\mathbf{m}^2\mathbf{m}$	SD-SAM	
			[100]	$^2\mathbf{m}^1\mathbf{m}^2\mathbf{m}$	SD-SAM	
230	Sr ₂ Fe _{1.9} Cr _{0.1} O ₅	1.410	[010]	$^2\mathbf{m}^1\mathbf{m}^2\mathbf{m}$	SD-SAM	

No.	Material entry	Index	Normals	Surface spin	Laue group	Surface character
231	<chem>Sr4Fe4O11</chem>	0.401	[001] [100]	$^2m^1m^2m$ $^2m^1m^2m$	SD-SAM SD-SAM	
232	<chem>Sr2Fe3S2O3</chem>	1.625	[001] [100] [010]	$^2m^1m^2m$ $2/m$ $2/m$	SD-SAM AFM AFM	
233	<chem>Sr2IrO4</chem>	1.3	[001] [010]	$^2m^2m^1m$ $^2m^1m^2m$	<i>d</i> -wave SD-SAM	
234	<chem>SrMn2As2</chem>	0.482	[110] [100] [010]	$^22_z/2m_z$ $^22_z/2m_z$ $^22_z/2m_z$	SD-SAM SD-SAM SD-SAM	
235	<chem>Sr2Mn3As2O2</chem>	0.212	[001] [100] [110] [010] [110]	$^24/1m^1m^2m$ $^2m^1m^2m$ $^2m^2m^1m$ $^2m^1m^2m$ $^2m^2m^1m$	<i>d</i> -wave SD-SAM <i>d</i> -wave SD-SAM <i>d</i> -wave	
236	<chem>SrMnBi2</chem>	0.73	[001] [100] [110] [010] [110]	$^24/1m^1m^2m$ $^2m^1m^2m$ $^2m^2m^1m$ $^2m^1m^2m$ $^2m^2m^1m$	<i>d</i> -wave SD-SAM <i>d</i> -wave SD-SAM <i>d</i> -wave	
237	<chem>SrRu2O6</chem>	1.186	[001] [110] [120] [210]	$^1\bar{3}^2m$ $2/m$ $2/m$ $2/m$	<i>i</i> -wave AFM AFM AFM	
238	<chem>SrRu2O6</chem>	1.569	[001] [110] [120] [210]	$^1\bar{3}^2m$ $2/m$ $2/m$ $2/m$	<i>i</i> -wave AFM AFM AFM	
239	<chem>TbB4</chem>	0.469	[001]	$^2m^1m^2m$	SD-SAM	
240	<chem>TbCr2Si2</chem>	0.518	[001] [100] [110] [010] [110]	$^24/1m^1m^2m$ $^2m^1m^2m$ $^2m^2m^1m$ $^2m^1m^2m$ $^2m^2m^1m$	<i>d</i> -wave SD-SAM <i>d</i> -wave SD-SAM <i>d</i> -wave	
241	<chem>TbCu0.4Ge2</chem>	0.569	[100]	$^2m^1m^2m$	SD-SAM	
242	<chem>TbGe2</chem>	0.343	[001] [100]	$^2m^1m^2m$ $^2m^1m^2m$	SD-SAM SD-SAM	
243	<chem>TbMn2Ge2</chem>	1.694	[100] [110] [010] [110]	$^2m^1m^2m$ mmm $^2m^1m^2m$ mmm	SD-SAM AFM SD-SAM AFM	
244	<chem>TbMn2Si2</chem>	1.468	[100]	$^2m^1m^2m$	SD-SAM	

No.	Material entry	Index	Normals	Surface spin	Laue group	Surface character
			[110] [010] [110]	<i>mmm</i> ${}^2m^1m^2m$ <i>mmm</i>	AFM SD-SAM AFM	
245	TbNi _{0.4} Ge ₂	0.568	[100]	${}^2m^1m^2m$	SD-SAM	
246	TbNiGe ₂	0.566	[100]	${}^2m^1m^2m$	SD-SAM	
247	TbNiSi ₂	0.910	[100]	${}^2m^1m^2m$	SD-SAM	
248	Tb ₂ Ni ₃ Si ₅	1.368	[001]	${}^2m^2m^1m$	<i>d</i> -wave	
249	TbPO ₄	0.467	[100] [010]	${}^2m^1m^2m$ ${}^2m^1m^2m$	SD-SAM SD-SAM	
250	TbRuAsO	0.452	[110] [110]	${}^2m^1m^2m$ ${}^2m^1m^2m$	SD-SAM SD-SAM	
251	ThCr ₂ Si ₂	0.466	[001] [100] [110] [010] [110]	${}^24/1m^1m^2m$ ${}^2m^1m^2m$ ${}^2m^2m^1m$ ${}^2m^1m^2m$ ${}^2m^2m^1m$	<i>d</i> -wave SD-SAM <i>d</i> -wave SD-SAM <i>d</i> -wave	
252	ThMnAsN	0.922	[001] [110] [110]	${}^24/1m^1m^2m$ ${}^2m^2m^1m$ ${}^2m^2m^1m$	<i>d</i> -wave <i>d</i> -wave <i>d</i> -wave	
253	ThMnAsN	0.923	[001] [110] [110]	${}^24/1m^1m^2m$ ${}^2m^2m^1m$ ${}^2m^2m^1m$	<i>d</i> -wave <i>d</i> -wave <i>d</i> -wave	
254	ThMnPN	0.920	[001] [110] [110]	${}^24/1m^1m^2m$ ${}^2m^2m^1m$ ${}^2m^2m^1m$	<i>d</i> -wave <i>d</i> -wave <i>d</i> -wave	
255	ThMnPN	0.921	[001] [110] [110]	${}^24/1m^1m^2m$ ${}^2m^2m^1m$ ${}^2m^2m^1m$	<i>d</i> -wave <i>d</i> -wave <i>d</i> -wave	
256	Tl ₃ Fe ₂ S ₄	0.801	[010] [100]	${}^22/2m$ ${}^22/2m$	<i>d</i> -wave <i>d</i> -wave	
257	TmMn ₂ Ge ₂	1.690	[100] [110] [010] [110]	${}^2m^1m^2m$ <i>mmm</i> ${}^2m^1m^2m$ <i>mmm</i>	SD-SAM AFM SD-SAM AFM	
258	TmMnO ₃	1.341	[001] [100] [010]	${}^2/m$ ${}^22/2m$ $\bar{1}$	AFM <i>d</i> -wave AFM	
259	U ₁₄ Au ₅₁	0.282	[001]	${}^26/2m$	SD-SAM	
260	UBi ₂	0.378	[110]	${}^2m^1m^2m$	SD-SAM	

No.	Material entry	Index	Normals	Surface spin	Laue group	Surface character
			[110]	$^2m^1m^2m$	SD-SAM	
261	UGeSe	0.413	[100]	$^2m^1m^2m$	SD-SAM	
			[110]	$^2m^1m^2m$	SD-SAM	
			[010]	$^2m^1m^2m$	SD-SAM	
			[110]	$^2m^1m^2m$	SD-SAM	
262	UGeTe	1.425	[100]	$^2m^1m^2m$	SD-SAM	
			[110]	mmm	AFM	
			[010]	$^2m^1m^2m$	SD-SAM	
			[110]	mmm	AFM	
263	U ₂ N ₂ S	0.484	[110]	$^22_z/2m_z$	SD-SAM	
			[100]	$^22_z/2m_z$	SD-SAM	
			[010]	$^22_z/2m_z$	SD-SAM	
264	U ₂ N ₂ Se	0.485	[110]	$^22_z/2m_z$	SD-SAM	
			[100]	$^22_z/2m_z$	SD-SAM	
			[010]	$^22_z/2m_z$	SD-SAM	
265	U ₂ Ni ₂ Sn	1.479	[001]	$^{24/1}m^1m^2m$	<i>d</i> -wave	
			[100]	$2/m$	AFM	
			[110]	mmm	AFM	
			[010]	$2/m$	AFM	
			[110]	mmm	AFM	
266	U ₂ Ni ₂ Sn	1.200	[001]	$^{24/1}m^1m^2m$	<i>d</i> -wave	
			[100]	$2/m$	AFM	
			[110]	mmm	AFM	
			[010]	$2/m$	AFM	
			[110]	mmm	AFM	
267	UPt ₂ Si ₂	0.194	[110]	$^2m^1m^2m$	SD-SAM	
			[110]	$^2m^1m^2m$	SD-SAM	
268	U ₂ Rh ₂ Sn	1.103	[001]	$^{24/1}m^1m^2m$	<i>d</i> -wave	
			[100]	$2/m$	AFM	
			[110]	mmm	AFM	
			[010]	$2/m$	AFM	
			[110]	mmm	AFM	
269	VPO ₄	1.523	[001]	$2/m$	AFM	
			[100]	$^2m^2m^1m$	<i>d</i> -wave	
			[010]	$2/m$	AFM	
270	V ₂ WO ₆	0.966	[100]	$^22/2m$	<i>d</i> -wave	
			[110]	$^2m^1m^2m$	SD-SAM	
			[010]	$^22/2m$	<i>d</i> -wave	
			[110]	$^2m^1m^2m$	SD-SAM	
271	YBa ₂ Cu ₃ O ₆	1.420	[001]	$4/mmm$	AFM	
			[100]	mmm	AFM	
			[110]	$^2m^1m^2m$	SD-SAM	
			[010]	mmm	AFM	
			[110]	$^2m^1m^2m$	SD-SAM	
272	YBa ₂ Cu ₃ O _{6+δ}	1.4	[001]	$4/mmm$	AFM	

No.	Material entry	Index	Normals	Surface spin	Laue group	Surface character
273	YFe ₆ Ge ₆	1.634	[100]	<i>mmm</i>	AFM	
			[110]	<i>2m¹m²m</i>	SD-SAM	
			[010]	<i>mmm</i>	AFM	
			[110]	<i>2m¹m²m</i>	SD-SAM	
274	YFe ₆ Sn ₆	1.633	[001]	<i>2/m</i>	AFM	
			[010]	<i>2m¹m²m</i>	SD-SAM	
275	YMn ₂	1.746	[001]	<i>2/m</i>	AFM	
			[100]	<i>2/m</i>	AFM	
			[010]	<i>2z_z/2m_z</i>	SD-SAM	
276	YMn ₂ Ge ₂	1.691	[100]	<i>2m¹m²m</i>	SD-SAM	
			[110]	<i>mmm</i>	AFM	
			[010]	<i>2m¹m²m</i>	SD-SAM	
			[110]	<i>mmm</i>	AFM	
277	YMn ₂ Ge ₂	1.692	[100]	<i>2m¹m²m</i>	SD-SAM	
			[110]	<i>mmm</i>	AFM	
			[010]	<i>2m¹m²m</i>	SD-SAM	
			[110]	<i>mmm</i>	AFM	
278	YMn ₂ Ge ₂	1.496	[100]	<i>2m¹m²m</i>	SD-SAM	
			[110]	<i>mmm</i>	AFM	
			[010]	<i>2m¹m²m</i>	SD-SAM	
			[110]	<i>mmm</i>	AFM	
279	YMn ₂ Si ₂	1.495	[100]	<i>2m¹m²m</i>	SD-SAM	
			[110]	<i>mmm</i>	AFM	
			[010]	<i>2m¹m²m</i>	SD-SAM	
			[110]	<i>mmm</i>	AFM	
280	YMn ₂ Si ₂	1.469	[100]	<i>2m¹m²m</i>	SD-SAM	
			[110]	<i>mmm</i>	AFM	
			[010]	<i>2m¹m²m</i>	SD-SAM	
			[110]	<i>mmm</i>	AFM	
281	YbMnBi ₂	0.267	[001]	<i>24/1m¹m²m</i>	<i>d-wave</i>	
			[110]	<i>2m²m¹m</i>	<i>d-wave</i>	
			[110]	<i>2m²m¹m</i>	<i>d-wave</i>	
282	YbMnBi ₂	0.769	[001]	<i>24/1m¹m²m</i>	<i>d-wave</i>	
			[110]	<i>2m²m¹m</i>	<i>d-wave</i>	
			[110]	<i>2m²m¹m</i>	<i>d-wave</i>	
283	YbMnSb ₂	0.766	[001]	<i>24/1m¹m²m</i>	<i>d-wave</i>	
			[110]	<i>2m²m¹m</i>	<i>d-wave</i>	
			[110]	<i>2m²m¹m</i>	<i>d-wave</i>	
284	YbMn ₂ Sb ₂	0.483	[110]	<i>2z_z/2m_z</i>	SD-SAM	
			[100]	<i>2z_z/2m_z</i>	SD-SAM	
			[010]	<i>2z_z/2m_z</i>	SD-SAM	

No.	Material entry	Index	Normals	Surface spin	Laue group	Surface character
285	ZnV ₂ O ₄	1.24	[001] [1 $\bar{1}$ 0] [110]	$^22_z/2m_z$ $2/m$ $2/m$	SD-SAM AFM AFM	